Low Speed Wind Tunnel Flow Diagnostics and Benchmark Cases for Thermal Fluids CFD Validation Efforts

Paul J. Kristo[1], Saniya Sohail[1], Ryan S. Reed[1], Mark L. Kimber[2]

[1]Texas A&M University, College Station, TX 77840, USA
[2]Assistant Professor, Department of Nuclear Engineering and Department of Mechanical Engineering
AI Engineering Building 205D, Texas A&M University, College Station, TX 77840

ABSTRACT

A low speed, closed loop wind tunnel at Texas A&M University is presented for the study of turbulent mixing produced by a variety of flows types. Anticipated experiments range from canonical "unit flows" to more complex combinations of flows and geometries. Originally located at the University of Pittsburgh, the facility has since been re-located to the Thermal Hydraulics Verification and Validation (THVV) laboratory at Texas A&M University. The tunnel has undergone considerable modification and updated diagnostics prompting renewed interest in flow quality assessment. This includes a thorough mapping of the tunnel inlet velocity profile provided by Particle Image Velocimetry (PIV) measurements. Additional temperature and gage pressure measurements complete the assessment of system capabilities. These preliminary diagnostics yield empirically determined boundary conditions and fluid property correlations necessary for Computational Fluid Dynamics (CFD) model validation. The article concludes with the presentation of two unit flow types, including flow past a cylinder, with three distinct cross sections, and a single round jet in cross flow at three velocity ratios. The unit flows serve as initial benchmarks for THVV simulation efforts. Key validation metrics are presented for each benchmark including ensemble averaged velocities, Reynolds stresses, and proper orthogonal decomposition (POD) eigenvectors.

KEY WORDS
Computational fluid dynamics (CFD), Flow quality, Inlet boundary condition, Particle image velocimetry (PIV), Proper orthogonal decomposition (POD), Thermal fluids, Turbulence

1.0 INTRODUCTION

Originally conceived at the University of Pittsburgh [1, 2], the Thermal Hydraulics Verification and Validation (THVV) laboratory's low speed wind tunnel was moved to Texas A&M University in 2016. The tunnel's ongoing motive is to produce high fidelity thermal fluid experimental data for comparison to analogous computational models. The tunnel is capable of operation with or without the use of a free (or transverse) jet. Since its move, the laboratory has acquired several new diagnostics tools, which prompted a renewed interest in facility characterization and flow quality. For the experimentalist, immediate advantages of this report are a detailed overview of the retrofitting of the tunnel test section for improved model and measurement (intrusive and non-intrusive) accessibility, as well as proper quantification of system capabilities for accurate proposal of experimental conditions. Long term advantages of the report serve the computationalist, who will no doubt find several quantities of interest useful for computational fluid dynamics (CFD) modeling inputs. The article closes with two examples of validation data sets collected using the facility. The data sets provide two canonical flow types that are of interest in a current campaign involving more complex variations of these flows.

The current diagnostics treatment empirically confirms the analytical calculations that formed the basis of the tunnel's original design. This objective is coupled with the desire to produce a test section flow quality that is sufficient for experiments in the area of thermal fluid sciences and to address ongoing concerns or areas of improvement where needed. In general, the criteria for flow quality first and foremost implies low acoustic (noise) and vortical (turbulence) disturbance fields [3, 4]. It is highly desirable to keep these facility disturbances to a minimum to avoid unwanted responses in the test section and as artifacts in the test measurements. A common example would be the concern of turbulence and its influence on boundary layer transition found in lift-drag measurements [5]. Likewise, a typical culprit of acoustic noise is the flow motivation, i.e. the driving fan or blower. The driving mechanisms behind turbulence and noise generation are different and so too are their measurement. Given the current needs and available measurement equipment, acoustic treatments are deemed outside of the scope of the current evaluation.

Concurrent with the requirement for low disturbance, nonuniformities in the mean velocity and temperature must be minimized prior to the final suppression of turbulence. Ideally, at this location, the scale of the turbulence is comparable to the nonuniformities in mean velocity and temperature [3]. Spatial non-uniformities in velocity greatly affect the general flow field and transition processes that occur in the test section, including the evolution of wakes and shear layers, as well as aerodynamic forces imposed on models [6]. Likewise, in non-isothermal testing, temperature gradients and profiles are influenced by non-uniformities found upstream causing similar measurement bias.

While concerns over flow quality and carefully tuned experimental parameters constitute accurate depictions of the physics themselves, more modern treatments in verification, validation, and uncertainty quantification fully bridge the numerical connection. Indeed, a modern facility shakedown cannot afford to be without proper uncertainty quantification. Conventional probe measurements and their corresponding treatments have received considerable attention in years past, with an admirable treatment on the subject given by Moffat [7] that has influenced several standards in measurement science. Building upon this work, the current article promotes uncertainty calculations in accordance with the standards promoted by ASME [8, 9]. More recently, the lines between experiment and numerical algorithms have blurred, with the advance of non-obtrusive optical techniques such as particle image velocimetry (PIV). At the time of this writing, new methodologies for optical measurement uncertainty quantification are ongoing and will no doubt morph with new algorithm developments as well. As such, the suggestions of Oberkampf and Smith [10] are employed as a means of potential future use or adjustment of the current PIV results and uncertainty quantification.

2.0 EXPERIMENTAL DESIGN

A recommended first source is the comprehensive guide to low speed wind tunnel design and testing by Barlow et al. [11]. In application, the design rules of Mehta and Bradshaw [12] and the flow quality insights of Reshotko, Nagib, and Saric [3, 4] have proven to be invaluable resources for low disturbance tunnel design. Regarding experimental measurement and validation, the interested reader is highly encouraged to review the text of Coleman et al. [13], the standards promoted by ASME [9], and the paper by Oberkampf and Smith [10].

2.1 Facility

The closed loop, low speed wind tunnel facility is capable of velocities in the range of $9.52 \leq U_\infty \leq 33.02$ m/s, where U_∞ is the freestream bulk velocity, calculated according to the two-dimensional spatially integrated mean of the respective plane. The tunnel test section measures $609.6 \times 457.2 \times 217.7$ mm, corresponding to its length, width, and height, respectively. Corresponding inlet Reynolds numbers range from $3.16 \leq Re_\infty \leq 8.53 \times 10^5$. In total, the tunnel's footprint is 7.1×1 m and stands 1.9 m high. An isometric view of the full Computer Aided Design model is presented in Figure 1.
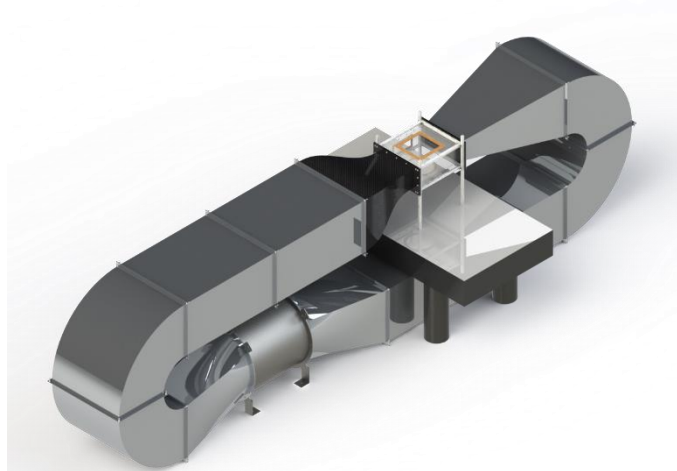
Figure 1: Isometric view of low speed wind tunnel.

Referencing Figure 2, the flow is motivated by a Greenheck Mixed Flow Fan Model QEI-22-I-50 with an internal diameter of 771.652 mm. The fan houses seven blades and twelve stators, with an additional three counter rotated stators at the three, seven, and eleven o'clock position. The fan was selected for its favorable low sound (inlet sound power = 77 dBa, outlet sound power = 79 dBa), high efficiency (static efficiency of 29%), return air design. A 3.73 kW induction motor, capable of 1839 rpm maximum speed, powers the fan. The motor assembly is external from the fan casing and employs a belt drive configuration, minimizing heat transfer from the motor to the freestream and negating any potential acoustic disturbances. The motor is controlled by a Yaskawa Z1000 variable frequency drive with a 100:1 turndown ratio, and ±0.01 RPM resolution. The fan is directly mounted (fixed) to the floor, with each foot employing a 19.05 mm thick rubber pad for vibrational dampening.
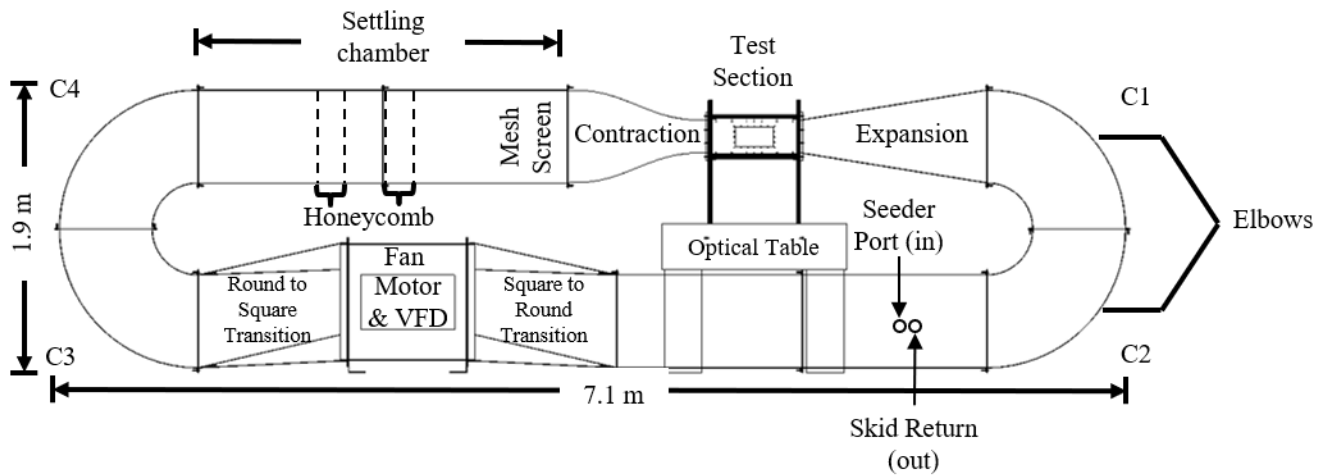
Figure 2: Front view of low speed wind tunnel.

From the fan, the flow moves in the clockwise direction (Figure 2) first through a round to square (rectangular) transition. This rectangular interface measures 914.4×609.6 mm and constitutes the internal cross section of the tunnel, excluding the fan, transitions, and test section itself. Unless otherwise noted, the primary ducting material for the facility is nominal 3.175 mm stainless steel. Continuing along the flow path, the next interface includes a 180° duct which routes the flow towards the upper half of the upright tunnel.

The flow then traverses through a 2.4384 m settling chamber. Inside this chamber are two identical aluminum honeycomb layers, with nominal cell diameters of 25.4 mm and a cell length/diameter ratio of 8. A galvanized steel mesh screen is placed at the end of the settling chamber with a wire diameter of 0.51 mm, nominal square aperture of 2.03 mm^2, 3.937 wires/cm, constituting a 64.0% open area. The honeycomb layers and screen dimensions were specified with the recommendations provided by [12, 14, 15].The final conditioning element before the test section is a contraction, also referred to as a nozzle. The contraction serves to reduce turbulence intensity by accelerating the flow and ensures reduced velocity gradients, minimizing turbulent anisotropy in the test section [5]. The contraction is composed of 2×2 weave carbon fiber weaves whose curvature incorporates a fifth order polynomial in both the spanwise and transverse directions, as originally promoted by [12, 16]. The nozzle tapers the flow from the larger tunnel cross section to that of the test section across its 0.9144 m length. The tunnel ducting and test section cross sections constitute a contraction ratio (inlet to outlet area) of 8.47 across the device. The flow conditioning elements have been carefully designed and placed to introduce highly uniform velocity and low turbulence conditions into the test section.

As previously mentioned, the test section inlet is 457.2×217.7 mm and is 609.6 mm in length. The test section walls consist of 9.525 mm thick polycarbonate with three of the four sides incorporating window cutouts and the fourth devoted solely to optical accessibility. The bottom (floor) window consists of a nominal 292.1 mm diameter cutout. The large field of view enables optical access and the circular shape provides variability in model mounting (i.e. aerodynamic sting or rake) at discrete 22.5° intervals. The side wall incorporates a rectangular window of 254×127 mm for wall mounting needs (i.e. cylinders, such as the work of Shafi et al. [17]). The top (ceiling) incorporates a large square cutout with a side length of 317.5 mm. The ceiling cutout is meant to provide a flexible "adapter" plate to other test section inserts and experiments such as the turbulent jet investigations of Reed et al. [18] and Lewandowski et al. [19]. All test section wall and window interfaces have been carefully machined and properly sealed to prevent unwanted boundary layer interactions or leakages from the system, while minimizing optical inaccessibility. As a final precaution for optical measurements, external matte black foam cutouts, sized for each test section wall, are available to block out unwanted ambient lighting during testing.

The test section frame is composed of 8020 aluminum allowing for a variety of framing solutions for future experimental needs. Each framing leg uses a 3.175 mm rubber dampener. The test section is free floating on a large Newport RS2000-48-12 Optical Table with S-2000 Stabilizer$^{\text{TM}}$ Vibration Isolators. The dampeners, table, and isolators act to reduce unwanted vibrational coupling promoted by the tunnel on the diagnostic equipment.

The outlet of the test section is mated to a linear expansion, which acts to properly expand the flow back to the larger tunnel ducting cross section and limit any unwanted back pressure effects in the test section area. The flow is then rerouted back to the fan via a secondary 180° elbow, straight duct, and square to round transition, completing the closed loop system. The square to round transition is identical to the previously mentioned round to square transition found on the front of the fan. Taylor et al. [20] have previously examined the streamwise and cross-stream velocities in a square to round transition duct using laser doppler velocimetry. They reported that streamwise boundary layers incur smaller thicknesses away from the fillets of the transition duct and that secondary velocities occur as a result of cross-stream pressure gradients formed by the longitudinal curvature of streamlines passing through the transition. These effects promote unsteadiness in the immediate region upstream and downstream of the fan which can ultimately propagate to the test section. These behaviors will be investigated further in Section 3.2. As denoted in Figure 2, there are two dedicated 1 in NPT ports available for PIV seeder particle injection and the "skid return". This second port refers to a secondary heat and flow control system

affectionately referred to as the "skid". The modular system is typically employed for jet in cross flow studies, where the flows are generated by the skid and wind tunnel, respectively. A separate design and flow diagnostics report on this facility is currently in development.

2.2 Instrumentation

2.2.1 Time-Resolved Particle Image Velocimetry

Major components of the particle image velocimetry system include a pair of high-speed cameras, a dual-pulse laser, and seeding particle generator. The cameras are both Phantom Miro M120's with a 12-bit dynamic range and maximum resolution of 1920×1200 pixels. Each camera utilizes a Nikon AF NIKKOR 50 m f/1.8D lens and a LaVision Inc. 527 nm lens filter with 10 nm band pass and 70% transmission efficiency. For two-dimensional measurements, the laser sheet is generated by a Photonics Industries DM30-527-DH laser with a maximum power of 60 mJ/pulse at 527 nm. The laser sheet thickness is approximately 1.0 mm with the minimum thickness carefully aligned with the center of the field of view, in this case the centerline of the tunnel test section. The seeding particles are Dioctyl Sebacate, which has favorable properties including non-toxic and evaporation at moderately high temperatures. The particles are introduced into the flow using a TSI Six Jet Atomizer Model 9306 with only two of the seeder jets utilized in conjunction with an air compressor. Typical settings for the compressor include a regulated pressure of 60 psi for 2-6 seconds per measurement. The PIV system captures velocity fields in major planes, producing inlet profiles along the height and width of the test section. Several key parameters regarding the camera setup, and data acquisition are summarized in Table 1. In total, five distinct slices are measured across both the xy and xz planes, providing an extensive look at the inlet hydraulic behavior. These width and height velocity fields constitute the xy and xz-planes, respectively, where x represents the streamwise flow direction. The calibration measurements are performed across the entirety of the tunnel's operating spectrum and are controlled via the motor variable frequency drive. Particular emphasis is placed on the centerline profiles, with six repeatable trials in the xy center plane and twelve repeatable trials in the xz center plane.

Table 1: PIV setup and data acquisition parameters for tunnel diagnostics

Acquisition Parameter	xy Plane	xz Plane
Number of Cameras	2	1
Camera Configuration	Mono (stitched)	Mono
Sampling Frequency [Hz]	1000	1000
Sampling Time [sec]	2.48	2.97
Fit Model	Pinhole	Pinhole
RMS of Fit	0.239622 0.264949	0.28104
Scale factor [px/mm]	6.84424 6.63192	5.38057
Focal Length [mm]	62.5972 61.326	61.5695
Field of View [px $\times$ px]	1920 x 432 1920 x 432	576 x 1200

The images are processed using LaVision DaVis 8.4.0 and consists of three primary stages: image pre-processing, vector processing, and post-processing. At the most fundamental level, the pre-processing stage serves as a last numerical filter to differentiate the seeding particles' intensity from an ideally uniformly black background. This, in conjunction with a carefully designed experiment (black background, little to no ambient lighting, uniform laser pulsing, and bandwidth filters) prime the images for vector field generation. The vector field processing step takes the raw images and converts them to instantaneous velocity vector fields mapped onto a square, regular Cartesian grid in Eulerian space. Post processing is performed in two parts. The first serves to remove any clearly erroneous vector fields. At this step, the data is not compromised in any way and still represents the true measurement. As a result of the first step of post processing, the vector fields may have missing information, visually seen as "holes" in the vector fields. For analysis involving the temporal dynamics of the fluid flow, this is less than ideal. To this end, a second post processing step is performed that interpolates empty spaces using the vector location's immediate neighbors. Ensemble statistics are then calculated for both the first and second post-processed vector field data sets. The first post processed set is used for ensemble statistics and uncertainty calculations while the second is used explicitly for analyses that are highly sensitive to temporal behavior. The full details regarding these three major steps are provided in Table 2.

Table 2: DaVis algorithms and options.

Step	Process	Description
1	Pre-Processing Subtraction Filter	• Butterworth High Pass Filter Filter length = 7 images
2	Processing Vector Calculation: Double Frames (PIV)	• Vector Calculation Parameter: Cross-Correlation Iterations: Multi-pass (decreasing size) Window size=64x64; Weight=Square 1:1; Overlap=75%; Passes=2 Window size=32x32; Weight=Circle 1:1; Overlap=75%; Passes=4 Options Enabled: Image correction; Calculate uncertainty; High accuracy mode for final passes • Multi-pass options Initial window shift for image reconstruction (first pass only)=Constant Correlation function" All initial pass(es): 'standard' I1*I2 (via FFT, no zero-padding) Final pass(es): normalized (I1-I1avg)*(I2-I2avg)/Stdev Deformed interrogation windows: Symmetric shift (both frames) • Multi-pass processing Peak ratio Q < 2 2x Median filter: remove and literately replace (>2 Stdev, <3 Stdev dev)
3.1	Vector Post Processing	• Allowable vector range: Vx: 0 +/- 1.5Ub; Vy: 0 +/- 0.5Ub;
3.2	Vector Post Processing	• Enable: Fill-up empty spaces (interpolation)

PIV measurements pose an interesting challenge in that the velocity fields are a function of both physical or analog observation and numerical computation. The fundamental PIV algorithm matches two consecutive images to compute a displacement field $dx(x, y)$ as the best fit (denoted by *) between the first image intensity $I_1(x, y)$ and second image intensity $I_2\big(x + dx(x, y), y + dy(x, y)\big) = I_2^*(x, y)$ via maximizing their correlation given by the sum $(I_1 I_2^*)$. Several renditions and modifications to this fundamental basis have been proposed and implemented over thirty years of PIV research, however most of the significant work in PIV uncertainty quantification has only occurred within the past ten years. Recently, Schiacchitano et al. [21] have utilized a dedicated experimental data base provided by Neal et al. [22] to assess four leading uncertainty quantification methods. Their work concluded that for first order statistics, the most accurate method was the correlation statistics method of Weineke [23], summarized here.

Given two consecutive PIV images, or an image pair, the second image intensity, $I_2(x)$, is dewarped onto the first, $I_1(x)$, using the computed displacement field, $u(x)$. This provides two nearly identical matching images whose correlation function is defined by Equation (**1**).

$$C(u) = \sum \big(I_1(x, y) I_2(x + u, y)\big) = \sum \big(I_1(x, y) I_2^*(x, y)\big) \tag{1}$$

It is assumed that the PIV algorithm is converged such that the correlation function is a maximum when $dC/du=0$. Thus, small differences $\pm \Delta x$ from the correlation peak should be identical regardless of their sign (+ or -). In the event of a non-zero slope, an iterative predictor-corrector scheme analyzes differences in the correlation function by shifting the peak of correlation function via $u + \delta u$ with δu shown explicitly in Equation (2). Each iteration is considered equivalent to an extra step of the PIV algorithm.

$$\delta u = \frac{\Delta x}{2} \frac{\log(C_+) - \log(C_-)}{2 \log(C_0) - \log(C_+) - \log(C_-)} = f(C_0, C_-, C_+) \\ = f\left(C_0, C_\pm - \frac{\Delta C}{2}, C_\pm + \Delta C/2\right) \tag{2}$$

It is convenient to prescribe shifts in the correlation peak according to (3).

$$\Delta C = \sum \Delta C_i = \sum \big(I_1(x, y) I_2^*(x + \Delta x, y) - I_1(x + \Delta x, y) I_2^*(x, y)\big) \tag{3}$$

Each term ΔC_i is an elemental contribution to the total correlation difference. The standard deviation of $\Delta C = \sum \Delta C_i$ is related to the covariance matrix of the particle positions in each frame ($\Delta C_{x1,y1}$ and $\Delta C_{x2,y2}$) and requires that each ΔC term has a zero mean. The auto-covariance term is non-zero inside a small neighborhood given by the particle image diameter and outside of this region the autocorrelation drops to zero. This allows for the typical 4D sum of the covariance matrix to be rewritten as a 2D sum over the distances Δx and Δy as seen in Equation (4).

$$\sigma_{\Delta C}^2 = n^2 \sum_{\Delta x \Delta y} cov\left(\Delta C_{x,y} \Delta C_{x+\Delta x, y+\Delta y}\right)$$

$$= \sum_{\Delta x \Delta y} \sum_{x,y=1}^{n} \left(\Delta C_{x,y} \cdot \Delta C_{x+\Delta x, y+\Delta y}\right) \tag{4}$$

$$= \sum_{\Delta x \Delta y} S_{\Delta x \Delta y}$$

The correlation statistics method then calculates the systematic uncertainty, b_i, according to Equation (5).

$$b_i = \sigma_u = f\left(C_0, C_\pm - \frac{\sigma_{\Delta C}}{2}, C_\pm + \sigma_{\Delta C}/2\right) \tag{5}$$

The correlation statistics method as described above applies to single variable uncertainties in the PIV measurement. These include the instantaneous velocity components, their respective means, and vector magnitudes which are directly measured and inferred. In turbulence, there are numerous statistical and instantaneous quantities of interest derived from the velocity fields, who have corresponding propagated uncertainties, such as the standard deviation, its magnitude, variance/covariance (Reynolds stresses), turbulence intensity, turbulent kinetic energy, vorticity, etc. The PIV uncertainty quantification is further complicated by the spatio-temporal resolution and elapsed time of the measurement which for most existing systems is limited to low sampling rates (~15 Hz) over large time periods, or time-resolved systems which sample at much higher speeds (≥1 kHz) over short time periods.

Recent efforts by Sciachhitano and Wieneke [24] have provided a framework for propagating instantaneous measurement uncertainty to derived quantities of interest using linear error propagation. They discuss that in the instance of correlated samples, the uncertainties of statistical properties are larger because the effective number of independent samples is smaller, yielding artificially high uncertainties. They propose the use of an effective number of samples, N_{eff}, as seen in Equation (6).

$$N_{eff} = \frac{N}{\sum_{n=-\infty}^{+\infty} \rho(n \Delta t)} \tag{6}$$

Where N is the total number of samples and $\rho(n \Delta t)$ is the autocorrelation of the independent samples. Computation of the effective number of samples is thus only deemed accurate if the longest flow fluctuations are captured several times. In the instance of purely uncorrelated data, the effective number of samples simply returns the original total number of samples, N. The interested reader is highly encouraged to review this paper for a full delineation of the uncertainty propagation of each statistical quantity of interest, considered too broad to include in the current review. The authors employed a commendable evaluation of the linear error propagation, including both existing experimental data and Monte Carlo simulations. They conclude that the uncertainty of time-averaged quantities are accurate to within 5%, whereas for Reynolds stresses accuracy is slightly larger at about 10%, and vorticity falling within 5-10% [24].

The current work's uncertainty propagation is faithful to methodologies discussed above, constituting the systematic uncertainty, b_i, in PIV measurements. To avoid any discrepancy in terminologies across different disciplines, let it be clearly stated: the author's choice to deem these uncertainties as systematic contributors is based on the definitions and standards proposed in the ASME V&V 20-2009 [9], which treats this unconventional uncertainty evaluation as a known, (directly quantified) measurement source. The random component of uncertainty, s_i, of the PIV measurements incorporates the repeatable trials mentioned previously for the centerline profiles. The values are calculated according to the student's t-distribution with 95% confidence and N degrees of freedom, where here N constitutes the number of trials [25]. Calculation of the random uncertainty component associated with each vector in the PIV field is displayed in Equation (7) using the streamwise component of velocity as the example metric. This formulation is intended for statistically derived quantities of interest, not instantaneous measurements.

$$\langle U \rangle \pm t_{N,P} s_{\langle U \rangle} = \langle U \rangle \pm \sigma_{\langle U \rangle} \tag{7}$$

Where $\sigma_{\langle U \rangle}$ constitutes the standard deviation of the means across each repeatable trial. With both the systematic and random components of the uncertainty known, the values are then combined via a root mean sum of the squares to form the total uncertainty in the metric according to Equation (8), again using the streamwise component of velocity as an example.

$$u_{\langle U \rangle} = \sqrt{b_{\langle U \rangle}^2 + s_{\langle U \rangle}^2} \tag{8}$$

The section concludes with a review of some of the current efforts and contributions in the area of PIV propagated uncertainty quantification. These efforts are not incorporated in the current work and are considered ongoing at the time of this writing. However, it is the authors' strong belief that these efforts, and those that follow, will be of significant benefit to the data sets presented in this work in the future and in re-evaluating the uncertainties of derived quantities as needed. A recent paper by Smith et al. reviews the applicability

of the effective number of samples. Smith states that accurate computation of the autocorrelation requires sufficiently long time records which based on their data, suggest a minimum of 20 integral time scales. Recent trends in time resolved PIV measurements, favoring high sampling rates and small physical time measurements, are questionable and may not achieve this requirement. The authors demonstrate that if the typical calculation of the integral time scale over the entire time record is used, the autocorrelation goes to zero. They suggest that, if a large time record exists, that the autocorrelation across subsets of the time record can provide more accurate depictions of the autocorrelation. Another critical finding is that the uncertainty in the mean of anti-correlated data is smaller for the same number of samples in comparison to the uncorrelated data, implying that the effective number of samples is *greater* than the total number of samples for anti-correlated data. To reiterate, the quest for accurate depiction of propagated uncertainties in PIV data is an ongoing and appreciably challenging area of measurement science. The results presented herein are amenable to future renditions and improvements. To the best of the authors' knowledge, the current uncertainty quantification methods are based on the most concrete methods available at the time of this writing.

2.2.2 Pressure Measurements

An Apogee Instruments Model SB-100 barometric pressure transducer provides the ambient pressure measurements. Ambient readings are external from the facility, in the laboratory environment and the sensor is housed in a protective cover to ensure no bias errors occur as a result of an unwanted breeze. Measurements are recorded with a National Instruments NI 9205 data acquisition unit. The device samples at 80 Hz for 3 seconds per measurement. Before the tunnel is turned on, the ambient pressure reading is collected, signifying that day's trial. Over six repeatable trials, the atmospheric pressure is found to be P_{amb}=102.341 $\pm$ 5.416 Pa or 1.023 bar. Systematic uncertainty contributors include the sensor's manufacturer curve fit, thermal drift, stability (long-term drift), and the data acquisition units' accuracy and resolution. The random component of uncertainty is provided by the six repeatable trials. The facility is located in College Station, TX, USA, about 103 m above sea level. For all practical purposes, the measured value is in excellent agreement with atmospheric pressure, and may be approximated as 1 bar.

The Omega Engineering Model PX409-2.5CGUSBH compound gage pressure transducer provides gage pressure measurements in the test section. The device is directly connected to the acquisition computer via USB, sampling for four minutes at 80 Hz per measurement. The sensor is connected to a bushing mounted on the ceiling of the test section at the x/L=0.875, y/W=0.389, z/H=0.5 location. The bushing interface has been carefully installed, mounted flush with the ceiling wall, and visually inspected to ensure no burrs obstruct the measurement readings. Before the tunnel is turned on, an initial measurement is recorded, to account for the DC offset in the sensor, subtracted from each measurement thereafter. Gage pressures are then collected for each measurement involved in the calibration procedure, where the motor operating frequencies are identical to the PIV measurements, mentioned prior. Six repeatable gage pressure calibration trials are performed with the test section completely evacuated. It should be noted that experiments incorporating geometric models in the test section induce additional pressure drop and such experiments should consider additional pressure measurements as necessary. Gage pressure results across the tunnel's operating spectrum will be discussed in greater detail in Section 3.3.

2.2.3 Temperature Measurements

Six type T thermocouples with a crushed ice bath reference point are calibrated against an Isotech Calisto 2250S Dry Block Calibrator with an Isotech Model 935-14-61 platinum resistance thermometer reference probe. The thermocouple voltages are recorded via a National Instruments NI 9213 data acquisition unit and the platinum resistance thermometer resistances are logged by an Isotech MilliK. The NI data acquisition unit and the MilliK logger are controlled via MATLAB and LabView, respectively and are triggered. The calibration procedure is automated and incorporates thirteen evenly spaced temperature setpoints in the range from 299.817 to 366.483 K. The automated procedure allows for the dry block calibrator to settle for 30 minute intervals, ensuring that each calibration point reaches a tightly controlled temperature value. Twelve repeatable trials have been executed to assess repeatability. A linear curve fit is then applied to each thermocouple, from which the maximum uncertainty in a given thermocouple was determined to be $\pm$ 0.8297 K.

An aerodynamic sting has been manufactured to position one of the thermocouples at the inlet to the tunnel test section without perturbing the flow. Another thermocouple is place externally from the tunnel to record ambient air in the laboratory environment. The remaining four thermocouples are then placed in two sperate configurations. The first configuration places the sensors at the inlet cardinal coordinates: North, South, East, and West with respect to the flow direction ("moving with the flow"). The other test positions the thermocouples on the corners of the inlet, namely North East, South East, South West, and South East. The motivations for these measurements are two-fold, the first being to determine the centerline steady state temperature of the tunnel across its operating spectrum. Five measurement points were conducted across the spectrum, where for a given test, the tunnel went from room temperature to a steady state temperature over the course of four hours with the thermocouples logging one-hundred samples for one second approximately every fifteen seconds. The final hour of each run constitutes the steady state condition from which these measurements are averaged, to formally produce the steady state centerline inlet temperature. The tunnel relies entirely on passive cooling to remove any undesired heat generation, i.e. as a result of frictional heating and these results directly quantify the significance. The second motivation takes advantage of the nine available inlet probe locations to produce a temperature mapping across the inlet plane. This information helps to assess modeling assumptions regarding the test section inlet temperature profile.

3.0 TUNNEL PERFORMANCE

With the facility and instrumentation fully defined, we now introduce the coordinate system and probe locations more formally in Figure 1. The x-, y-, and z-directions apply to the streamwise, spanwise, and transverse directions. The centroid of the coordinate axes is the center point on the inlet face. It should be noted that each of the three major measurement types are collected individually, i.e. on separate occasions, so that any perturbations to the flow caused by one sensor do not influence the measurements of another. Based on current experimental capabilities, this section serves to provide required hydraulic and thermodynamic flow quantities necessary to close governing equations of the thermal fluids experiments intended for this facility.
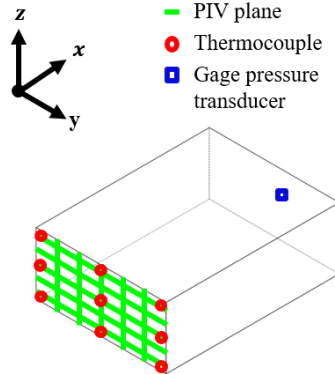

Figure 3: Tunnel diagnostics coordinate system and probe locations.

3.1 Inlet Velocity Calibrations

Streamwise velocity inlet profiles are provided in Figure 4 for both the xy and xz centerline planes with examples of the lowest and high motor operating frequencies. External framing around the test section inhibits laser light and optical access at the true inlet to the test section. Trustworthy results at nearly identical locations in each plane are found at the $x=29.6746$ mm and $x=30.2505$ mm locations, for the xy and xz planes, respectively. In general, conventional PIV is not well suited for boundary layer measurements and the near wall measurements need be treated with some level of scrutiny. Besides the camera resolution constraint, the laser poses physical reasons for this as well. The laser enters the test section in the -y and +z direction for the xy and xz planes, respectively. In general, the near wall measurements along the laser's entering side provide a slightly better signal than that on the exiting side, where laser energy is scattered by seeder particles in the test section and reflected by impact with the secondary (far) wall of the test section. These factors explain the increased uncertainty in the near wall regions for both sets of measurements. The freestream motion of the fluid however, is captured quite well and provides a good basis for calculating a bulk fluid motion, according to the integral mean, $U_\infty(x,y) = \int_{-y/2}^{y/2} U(x,y)dy / \int_{-y/2}^{y/2} dy$ for the xy-plane, and analogously for the xz plane.


(a) (b)
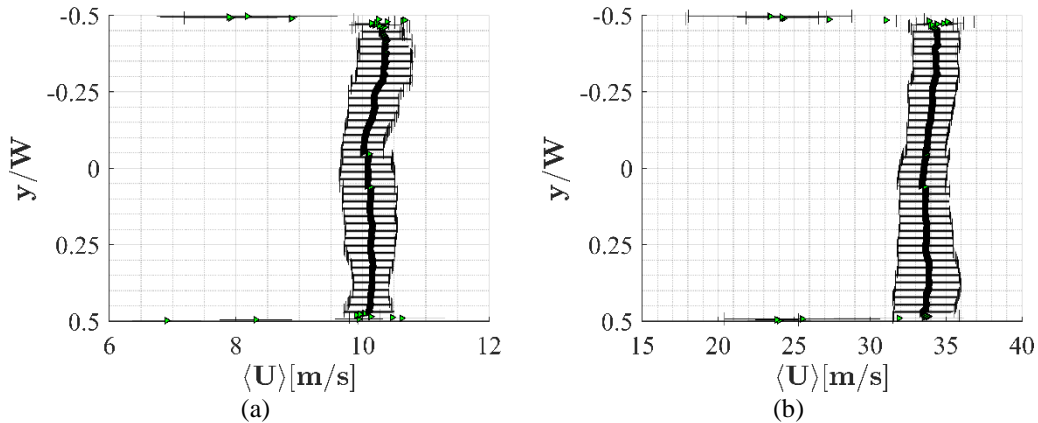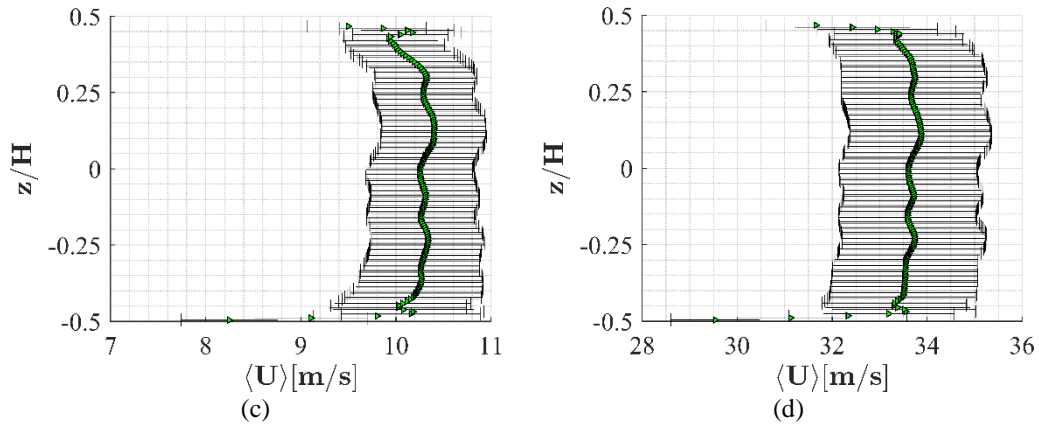
Figure 4: Test section inlet velocity profiles for xy plane (a) lowest and (b) highest speed and xz plane (c) lowest and (d) highest speed.

Applying this formulation to each measurement point in each of the two planes produces Table 3. The bulk freestream velocities in each plane are compared via a relative error, where the xz plane is considered the more trustworthy plane, as a result of one camera (no stitching needed) and better near wall accuracy as evident from Figure 4. The relative error reveals that the two measurement planes produce highly agreeable results, with a maximum difference of ~4%.

Table 3: Bulk inlet streamwise velocities across tunnel operating spectrum.

Motor Frequency, f_{VFD} [hz]	Bulk freestream velocity, $U_\infty(x,y)$ [m/s]	Bulk freestream velocity, $U_\infty(x,z)$ [m/s]	Relative error, $\epsilon = \dfrac{\|U_\infty(x,z) - U_\infty(x,y)\|}{U_\infty(x,z)}$
16.0	10.11	10.03	0.01
19.8	12.42	12.12	0.02
23.6	14.86	14.30	0.04
27.3	17.34	17.24	0.01
31.1	20.07	19.51	0.03
34.9	23.30	22.91	0.02
38.7	26.00	25.18	0.03
42.4	28.53	28.11	0.01
46.2	31.27	30.47	0.03
50.0	33.58	32.91	0.02

With freestream bulk velocities firmly established, all ten measurement points in each plane can be readily seen in their non-dimensionalized form according to Figure 5.


(a)

(b)
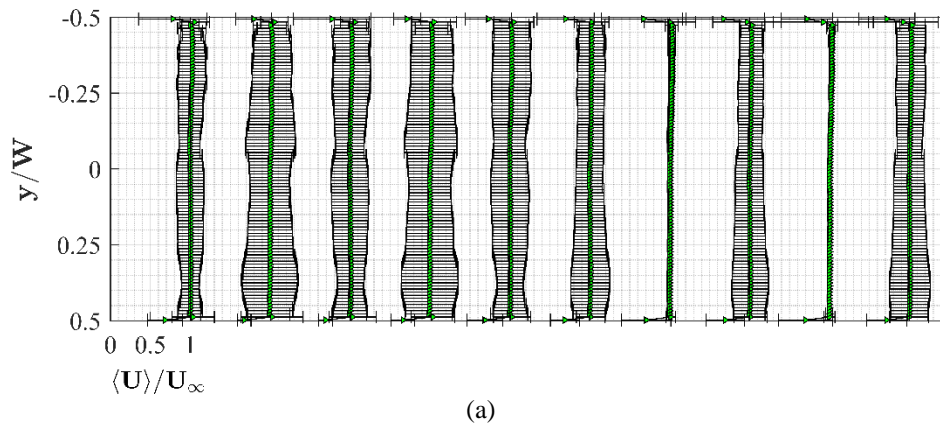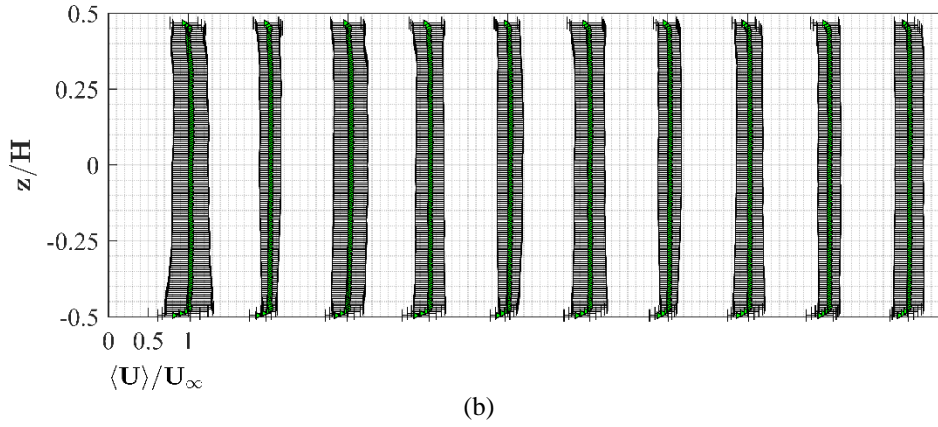
Figure 5: Non-dimensionalized streamwise velocity profiles for each calibration measurement in (a) xy plane and (b) xz plane. Note: uncertainties in both sub figures are scaled ×4 for visualization.

Table 3 also provides the basis for the inlet velocity calibration which yields a linear relation between the motor operating frequency, f_{VFD}, and the tunnel freestream bulk inlet velocity according to Figure 6(a) with corresponding deviation in Figure 6(b). The linear fit is applied to the "mean of means" across all available trials in the xz-plane, which is typically the primary plane of interest in experimental measurements for this test section. The linear fit produces an adjusted-R^2 value of 0.998 with a root mean square error of 0.3412. From Figure 6(b) it is evident that across all measurements, the maximum deviation is about ±0.5 m/s reaffirming the accuracy of the calibration.

(a)   (b)
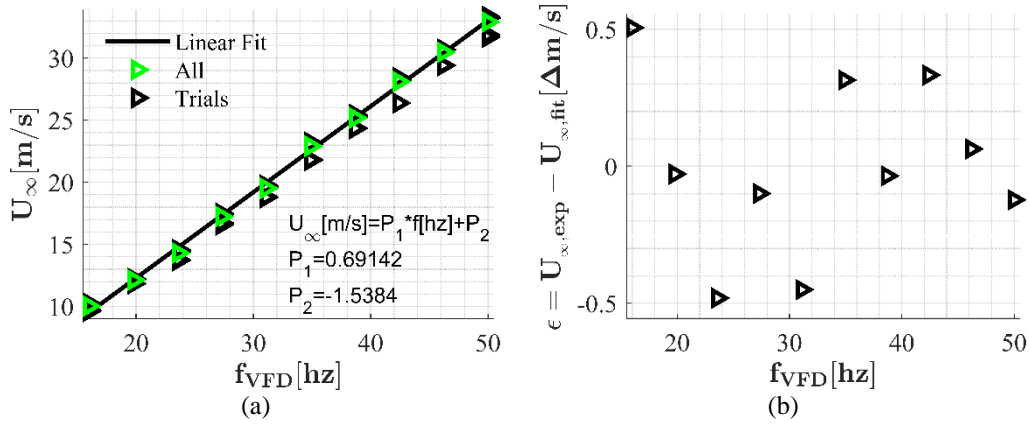
Figure 6: (a) Bulk free stream velocity calibrations across tunnel operating range and (b) deviation between measured and fitted values.

With established inlet velocity profiles and bulk freestream velocities valued well understood, we turn our attention now to the critical topic of inlet modeling. For turbulent flow in square nozzles in the low speed regime, a top hat profile is expected. Several flow conditioning elements have been implemented to meet this need as discussed in Section 2.1. Figure 4 and Figure 5 provide further quantified proof that the top hat profile is indeed appropriate. A thorough affirmation of the top hat profile however, is provided by assessing the five inlet traces in each place, encompassing the entirety of the test sections spanwise and transverse directions as seen in Figure 7. As stated earlier, conventional PIV systems are poorly suited for near wall measurements. It is expected that boundary layers for these locations will differ, as a function of the test section dimensions and corner proximity. Dular et al. [26] utilized Laser Doppler Velocimetry to confirm these observations with their water tunnel facility. If higher fidelity measurements in the near wall regions are needed, it may be worthwhile to pursue similar measurements with Laser Doppler Velocimetry or Hot-Wire Anemometry on the current facility as well. Overall, the current free stream profiles infer that a top hat inlet profile is indeed appropriate across the entirety of the tunnel's operating conditions.
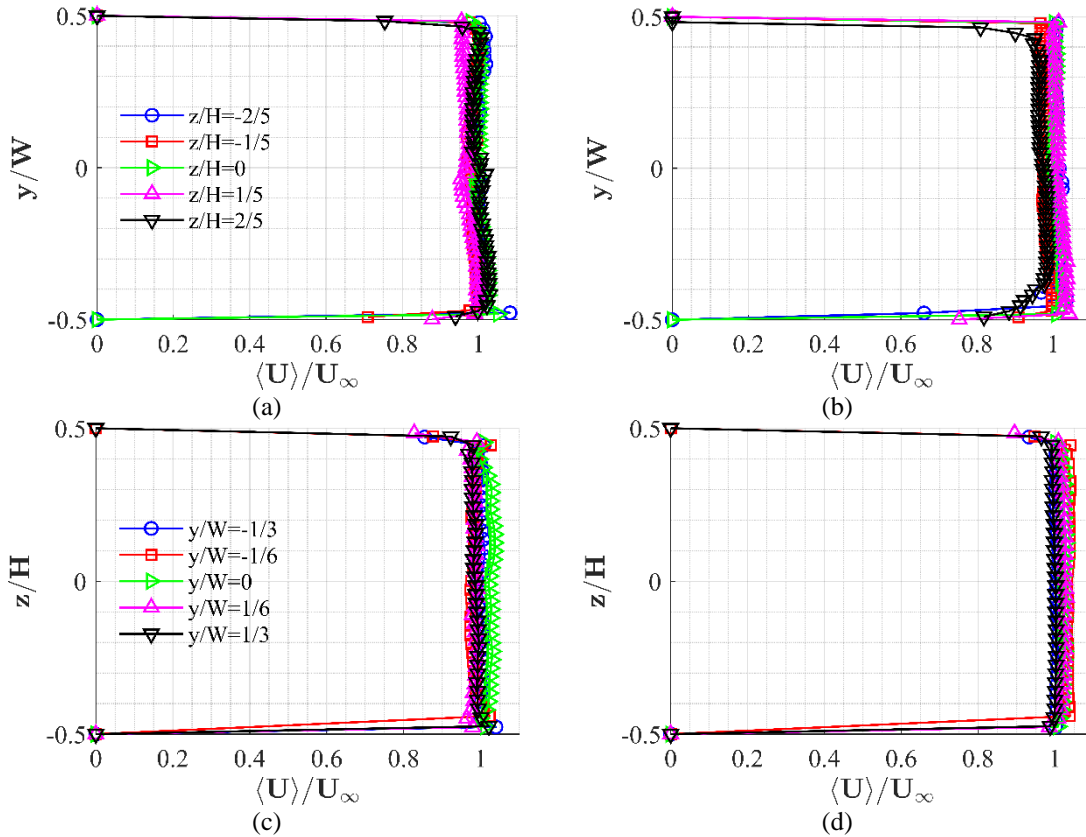
Figure 7: Collapsed streamwise inlet velocity profiles for xy plane (a) lowest and (b) highest speed and xz plane (c) lowest and (d) highest speed.

3.2 Unsteady flow effects

Inlet flow angularity is a critical metric in assessing the flow "steadiness". The angularity of the inlet flow also helps to assess the essential modeling assumption of a purely unidirectional flow, i.e. the streamwise component of velocity, $\langle U \rangle$, is the only non-zero mean velocity component at the inlet. Barlow at al. [11] have described the inlet flow angularity as an essential diagnostic for quantifying potential flow separations that may be occurring upstream in the tunnel and inadvertently affecting experimental results in the test section. Such irregularities can occur as a result of flow separation from the contraction, diffuser, and potential air leaks. Other sources of unsteadiness are promoted by rotating machinery elements: non-uniform inflow to the fan can be determined from the dominant frequencies matching the blade frequency or possibly harmonics. Mechanical vibration also promotes these affects and typically occurs at the fan speed. Thus, quantifying this "upflow" effect is useful in providing tunnel corrections for experimental results. One appreciable example is the correction of drag effects that may be aided or deterred by upflow. The concerned reader is advised to see Barlow et al.'s text on the subject for more details on this and other such corrections.

The PIV results have the advantage of providing thousands of vectors, collected synchronously, for comparison. The flow angularity for a given velocity vector can thus be determined simply from trigonometry according to, $\theta = \tan^{-1}(\langle V \rangle / \langle U \rangle)$, and analogously for components U and W. The current investigation focuses again on the xz plane which has the benefit of one camera, without stitching vector fields thereby compromising the true measurement in the overlapping region. The results of this computation are provided in Figure 8 for the minimum and maximum operating conditions. With the exception of three points in the lower portion of Figure 8(a), the inlet traces all appear to be within $\pm 1.2°$. The results are met with some scrutiny, where from Table 1 it can be seen that the scaling factor for the xz plane is 5.38057 px/mm. In this sense, the PIV system is again limited in its results, reflecting similar concerns as previously mentioned for the near wall region. In general, the assumption of a uni-directional inlet velocity is still considered reasonable from this current investigation and leaves room for future work with higher spatial fidelity measurements in the near wall regions.
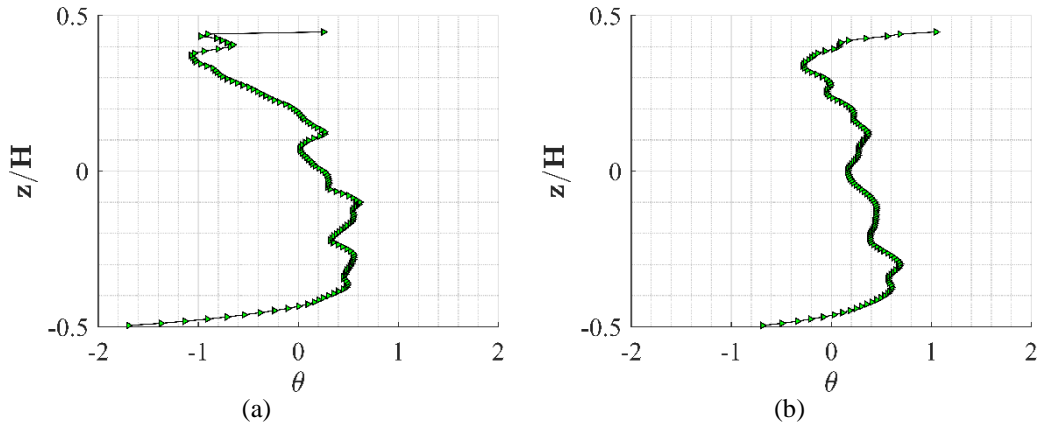
Figure 8: Flow angularity profiles in the xz plane for the (a) minimum and (b) maximum speed.

Next, the root-mean-square (RMS) velocity for the streamwise component ($=\sqrt{u^2}$) is examined. The RMS velocity, while lacking physical significance, borrows from the principles of signal analysis in electrical engineering to offer a first intuitive look into the turbulent energy content [27]. It is typically normalized by a bulk inlet velocity or centerline velocity to produce the well-known 'turbulence intensity'. Well established turbulence models usually require some quantification of the expected turbulent kinetic energy at the inlet, with the streamwise velocity component being the first and most essential metric to this end. As such, the turbulence intensities for each inlet profile across the entire operating spectrum are presented in Figure 9. The ideal profile at any given operating speed, consists of a flat (very low turbulence intensity) region in the freestream and two distinct and identical peaks in the near wall regions, where fluctuations are expected to be higher. Figure 9 presents these results with fixed axes limiting the turbulence intensity displayed to $\sqrt{u^2} \leq 25\%$, thereby exacerbating the local behaviors of turbulence intensities for inspection.
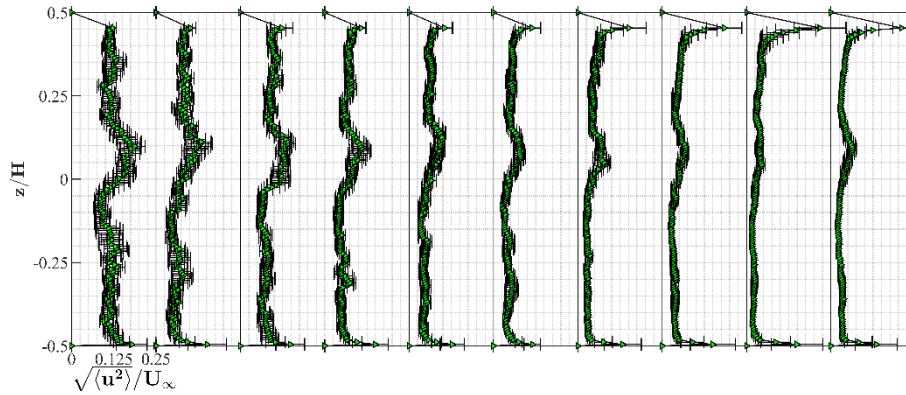

Figure 9: Turbulence intensity profiles for each calibration measurement in xz plane.

The same spatially integrated mean calculation used to calculate the freestream bulk velocities from the velocity profiles is now applied to the RMS velocity profiles from Figure 9 to produce Table 4. Present values are in the range of $3.99 - 11.77\%$, with turbulence intensity values being inversely proportional to operating speed. The large values occurring at low speeds are believed to be over-estimated as a result of the discrepancies in the current pulse timing utilized for high speed measurements. It is worthwhile to revisit these measurements with conventional PIV or hot-wire anemometry (longer sampling times at lower sampling rates) for improved estimates.

Table 4: Turbulence intensity inlet quantities.

VFD [hz]	$\left(\sqrt{\langle u^2 \rangle}\right)_\infty /U_\infty$	$\left(\sqrt{\langle v^2 \rangle}\right)_\infty /U_\infty$	$\left(\sqrt{\langle w^2 \rangle}\right)_\infty /U_\infty$
16.0	11.77%	5.67%	9.83%
19.8	7.41%	6.16%	7.19%
23.6	8.76%	4.28%	7.33%
27.3	6.29%	4.64%	5.84%
31.1	5.63%	3.45%	5.36%
34.9	5.07%	3.75%	4.37%
38.7	4.40%	3.38%	4.10%
42.4	4.73%	3.25%	4.15%
46.2	3.61%	3.23%	3.49%
50.0	3.99%	3.16%	3.60%

Streamwise velocity signals are extracted from the inlet centerline point in the xz plane for each calibration measurement point. The Fast Fourier Transform is calculated using the MATLAB 'fft' function, from which the power spectral density is computed. In reference to Figure 10, the five highest power spectral density magnitudes and corresponding frequencies are used to generate nose gates (green) for each measurement in comparison to the original unfiltered signals (black). High power spectral density content is observed at higher dominant frequencies for the maximum operating speed as compared to the minimum. This has been previously confirmed by Hunt et al. [28] and their Hot-Wire Anemometry measurements in the Vlebanoff-Saric low speed wind tunnel, a similarly sized facility appropriate for comparison here. The authors measured all three velocity components and confirmed that as tunnel speeds increases, low frequency peaks under 20 hz develop and grow in amplitude for the streamwise velocity component only.

(a)   (b)
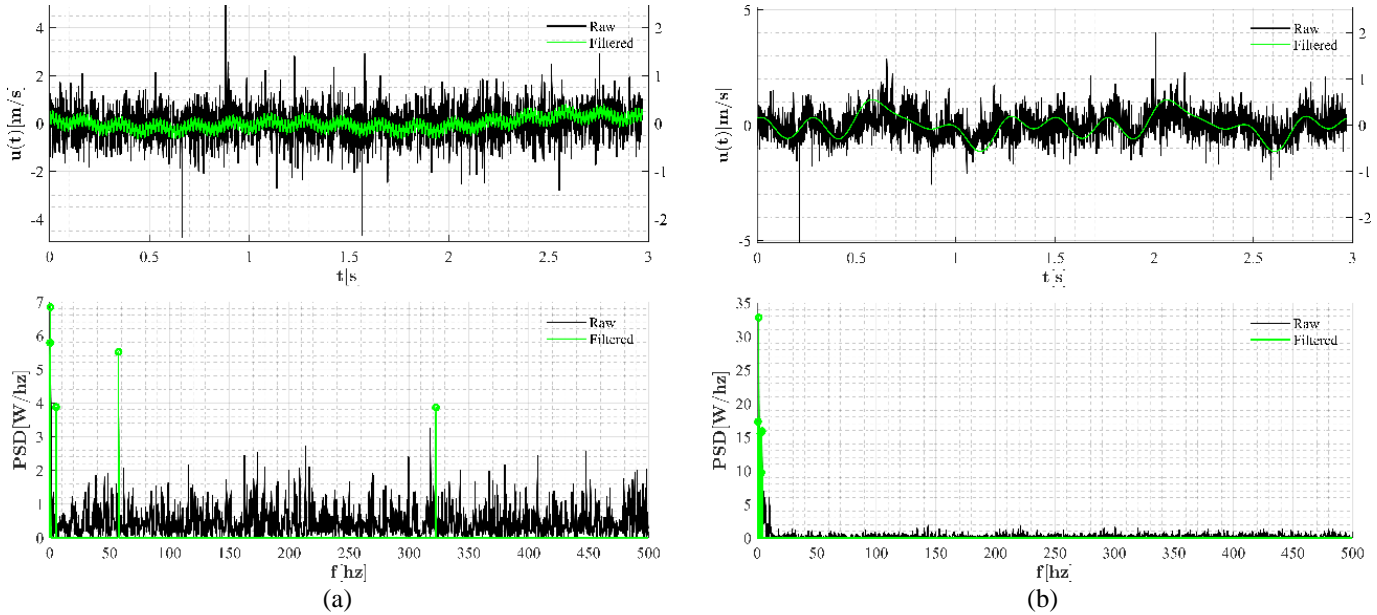
Figure 10: Raw and filtered (top) velocity signal and (bottom) power spectral density content for (a) minimum and (b) maximum operating speed. NOTE: For top profiles, left y-axis corresponds with raw signal and right y-axis corresponds with filtered signal.

From Table 5, it is clear that the current facility exhibits similar trends to that of [28]. For all motor operating frequencies up to f_{VFD}=27.3 hz, there exist dominant high frequencies present in the u centerline signal. With the exception of the f_{VFD}=19.8, all other measurements present in the range $16.0 \leq f_{VFD} \leq 27.3$ exhibit dominant frequencies that are an order of magnitude higher than those in the $31.1 \leq f_{VFD} \leq 50$ hz range. For the remaining operating frequencies tested, i.e. $f_{VFD} \geq$31.1 hz, the dominant frequencies are below 20 hz, without exception. These observations imply that for motor operating frequencies below f_{VFD} <31.1 hz, flow disturbances exist as a result of power, motor, blade passing, or stator passing frequencies and their harmonics [28]. Further investigation should seek to accurately measure all three velocity components and pressure fluctuations at the inlet with a minimum Nyquist frequency of 1 khz. This is most easily accomplished using a dual (cross) sensor hot-wire anemometer probe and pitot tube. If multiple such sensors are available, a rake formation is suggested. By comparing the power spectral density content of each signal and evaluating the temporal correlation of each signal with itself, the culprit(s) of higher disturbance intensities can be determined.

Table 5: Dominant frequencies (without parenthesis, f [hz]) and power spectral density content (with parenthesis, PSD [W/hz]) of streamwise fluctuating velocity component at each calibration point (bold row header, f_{VFD}[hz]).

16.0	19.8	23.6	27.3	31.1	34.9	38.7	42.4	46.2	50.0
0.67	0.34	0.67	1.01	1.01	2.02	1.01	2.36	1.35	1.35
(6.84)	(2.04)	(13.62)	(8.45)	(7.93)	(11.28)	(5.88)	(32.43)	(17.83)	(32.81)
0.34	1.01	0.34	0.34	0.34	1.68	3.70	11.78	0.67	0.67
(5.78)	(1.56)	(2.88)	(7.54)	(3.53)	(11.22)	(3.48)	(14.28)	(13.20)	(17.32)
57.58	0.67	25.25	1.68	2.69	0.34	1.68	5.39	10.77	4.04
(5.51)	(1.51)	(2.04)	(6.74)	(2.36)	(8.14)	(3.15)	(9.07)	(11.11)	(15.91)
5.39	2.02	133.00	0.67	3.03	7.41	6.73	4.38	4.38	2.69
(3.88)	(1.34)	(2.01)	(3.69)	(2.08)	(7.15)	(2.73)	(8.01)	(6.03)	(15.57)
322.56	54.55	116.50	295.29	4.38	0.67	7.07	1.01	1.68	3.37
(3.87)	(1.21)	(1.87)	(2.46)	(1.63)	(5.72)	(2.63)	(7.60)	(4.43)	(9.72)

3.3 Gage pressure calibrations

As seen in Figure 11(a), the gage pressure fits a second order polynomial curve fit, as expected, with an adjusted R-squared value of 0.99 and root mean square error of 3.60. For the evacuated test section, gage pressures in the range of $-48.59 \leq p_g \leq -517.40$ Pa are expected across the operating range of $16.0 \leq f_{VFD} \leq 50.0$ hz. Figure 11(b) shows that across the entire operating range, the deviation between measurement and the second order polynomial fit is within ± 5.8 ΔPa, with the maximum deviation occurring at $f_{VFD}=38.7$ hz. With knowledge of the ambient pressure from Section 2.2.2, total pressure inside the test section can also be calculated. The compound gage pressure transducer is capable of high-speed measurements (up to 1 khz) which prompts potential future avenues for assessing the unsteady behavior of the flow.
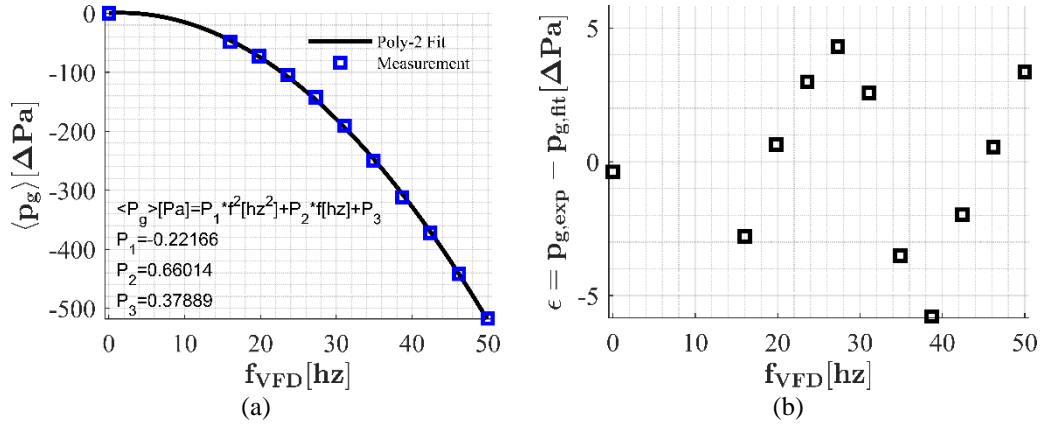

Figure 11: (a) Gage pressure calibrations in the evacuated test section across tunnel operation range and (b) deviation between measured and fitted values.

3.4 Inlet temperature calibrations

Temperature readings provide several benefits towards the overall tunnel diagnostics campaign. In general, properly quantified geometry, flow, pressure, and temperature measurements yield the minimum information necessary to fully constrain the thermal fluid problem. In lieu of a heat exchanger, the discrepancy between the ambient (external from tunnel) and test section inlet temperatures provides an empirical understanding of the heat generation from the tunnel's turbomachinery. This is paramount in assessing basic engineering assumptions (i.e. incompressible flow, ideal gas, and negligible heat generation) and in turn, the thermophysical properties of the working fluid (density, viscosity, specific heat, thermal conductivity, etc.). From Figure 12(a), the centerline inlet temperature follows a linear trend, as expected. The linear curve fit has an adjusted R-squared value of 0.97 and a root mean square error of 0.641. Figure 12 shows that across the operating range, the deviation between experiment and curve fit is within ± 0.66 K, with the maximum deviation occurring at $f_{VFD}=38.7$ hz, based on available measurements. The expected inlet centerline temperature across all measurements is $296.89 \leq \langle T_c \rangle \leq 305.97$ K, implying that the operating range fits within 10 ΔK. The results show that very little heat is added to the system, no doubt as a result of the exterior motor design and little frictional heating provided by the fan itself.
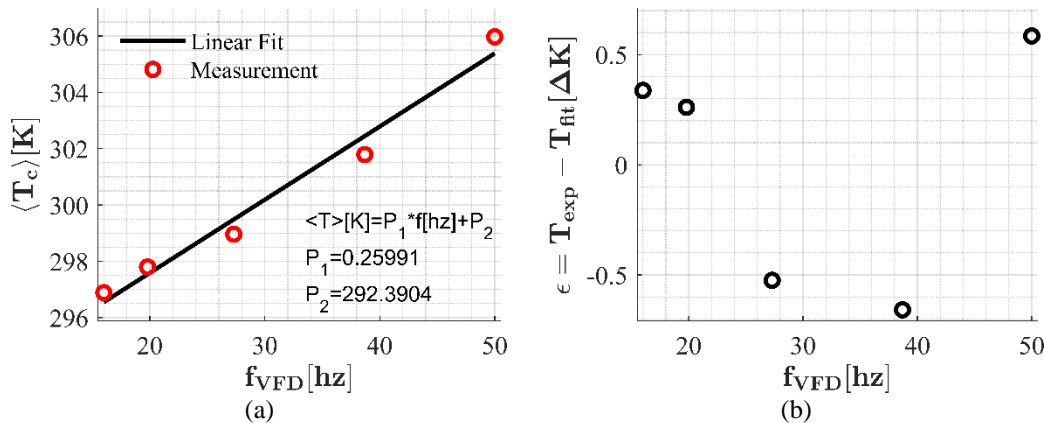

Figure 12: (a) Test section inlet centerline temperature calibration across tunnel operating range and (b) deviation between measured and fitted values.

To provide a truly comprehensive assessment of expected inlet modeling assumptions and properties of the flow, the temperature inlet profiles' spatial dependence is also required. Additional temperature measurements are conducted as described in Section 2.2.3 to fulfill this need. Results of the additional edge (near wall) probe measurements are revealed in Figure 13. The contours are generated using the nine (one centerline and eight major Cardinal coordinate points) probe locations and corresponding temperatures, mapped onto an artificial grid, and fitted using the surface fit rendition of MATLAB's 'fit' command with a second order polynomial

fit in both spatial directions (y and z). The current procedure neglects boundary layer effects and incorporates the minimum amount of spatial points capable of providing a reasonable spatial profile to meet the current objective (assessing modeling assumptions and properties of the flow). The results show a basic depiction of the spatial dependence of the temperature profiles and from Figure 13(a-b) and (c-d) it is clear that both of the inlet temperature profiles are within 1.2 K of their respective minimums and maximums. Based on the current inlet temperature profile results, and in conjunction with known pressures of the working fluid, modeling assumptions and thermophysical properties are now well informed for the experimental facility. With that said, the current temperature inlet profiles provide a coarse, if not rudimentary, approach that is subject to further scrutiny. Future work should consider the use of, i.e., a traversing cold wire anemometer probe to meet higher fidelity needs.
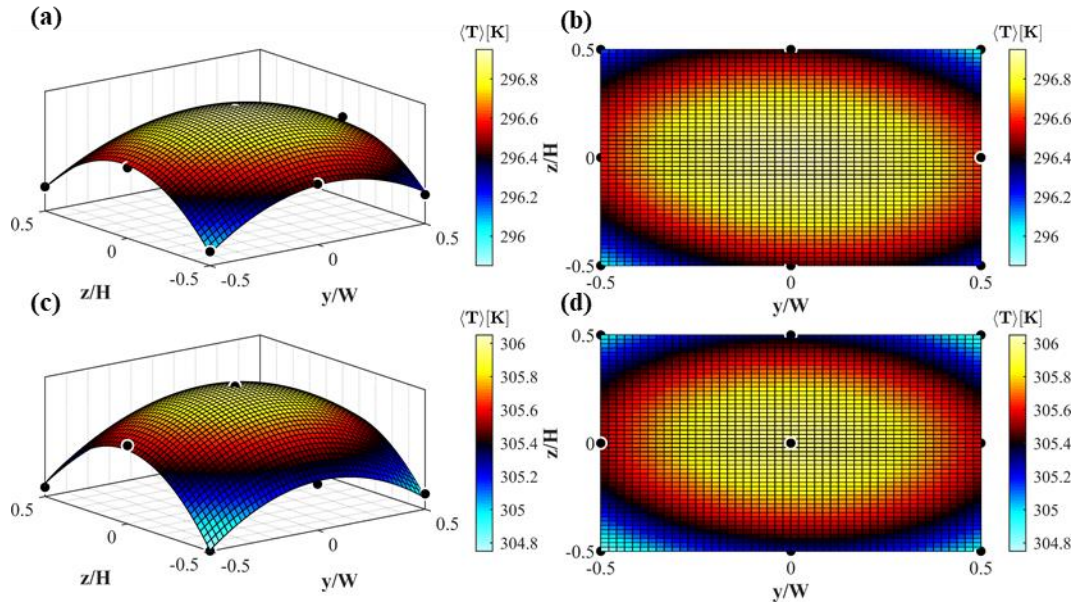
Figure 13: Interpolated tunnel inlet temperature contours consisting of (top row) minimum and (bottom row) maximum speed with (left column) isometric views and (right columns) planar views.

4.0 VALIDATION BENCHMARK CASES

Examples of key validation metrics are now provided via two canonical flow types measured with this facility. The two benchmark cases consist of flow past a cylinder and the round jet in cross flow. To be clear: a full validation study could be conducted on each of these sections, considered beyond the scope of the current work. This section merely serves as an introduction to the two flow types pertinent to current efforts in the laboratory. The experimental procedures are briefly reviewed with additional references provided for greater detail on the setup and acquisition procedures. Velocity, Reynolds stress, and proper orthogonal decomposition (POD) results are discussed for each benchmark case. The velocity and Reynolds stress profiles provide essential metrics rooted in the classical understanding of turbulence. POD provides a considerable first step in new and exciting developments in reduced order modeling, or more generally, data driven science. The clear objective in this section is to provide concise examples of validation worthy experimental results to aid in CFD modeling efforts and potential new and original contributions to these flow types' phenomenology, control, and prediction.

Recommended classical texts on the subject of turbulence include Bradshaw [27] and Pope [29]. Early works on the theoretical approach to proper orthogonal decomposition include that of Sirovich et al. [30-32] and Holmes et al [33]. The author has also found more recent works by Brunton et al. [34] and Kutz et al. [35] especially helpful in application and as introductory texts to data driven engineering.

4.1 Flow Past a Cylinder

Flow past a cylinder represents the simplest geometric case in a wider class of bluff body flows. These flows exhibit an arbitrarily shaped solid boundary that induces some type of flow separation promoting a rich set of responses in the near wall region and wake of the body. In the case of the round cylinder in a turbulent flow, a recirculation bubble exists directly behind the cylinder. This recirculation region and the turbulent boundary layer around the cylinder induce an oscillating Karman vortex street wake, the physics of which are highly dependent on the cylinder cross section and freestream Reynolds number. These behaviors represent one of the oldest and most rigorously analyzed flow types in the field of fluid mechanics and turbulence research. The ongoing challenge for such flows is finding an analytical expression(s) to accurately depict the wake vortex dynamics [36]. Indeed, only a brief synopsis of the possible physics is presented here; discussion of more specific geometries, flow types and additional physics sets would only serve to exacerbate the challenges presented in the current work.

In keeping with the commonly accepted convention for flow past a cylinder experiments, the coordinate system of the wind tunnel test section is modified as seen in Figure 14. Three cylinder geometries are tested including a round, square, and hexagonal cross section, each being 152.4 mm in length and having a hydraulic diameter of D_c=25.4 mm. Though less examined than its round counterpart, it is well known that the inclusion of corners and flat edges promoted by the square cylinder exhibit different near wall effects, namely reattachment, than that of the round cylinder, thereby also altering the wake formation [37]. Far less common in the literature are studies on the hexagonal cylinder, sometimes also referred to as an N=6-sided polygon. The hexagon experiments in the current work encompass the "corner orientation" in which the leading edge of the shape is a corner, as opposed to a wall. Sparrow et al. [38] have compiled empirically determined average Nusselt number information from the literature for a variety of non-circular cylinders, including the hexagon. Their compendium focused explicitly on heat transfer effects, providing improved surface-averaged Nusselt numbers for the geometries involved. Interestingly, the authors claim that the most relevant hexagonal experimental data to fit their needs was conducted in the 1930's by Hilpert [39] and that they were unable to find a more modern experimental data set. From the current author's literature review, the numerical works of Khaledi et al. [40] and Tian et al. [41] are the next most relevant hexagonal cylinder in a cross flow studies. Also of interest and to the best of the author's knowledge, none of the previously existing works have examined the behavior of the hexagonal cylinder at Reynolds numbers above 1×10^3.

Each cylinder is wall mounted at the centroid of the coordinate system. Two-dimensional, time-resolved PIV measurements are captured in the wake region of each cylinder at the z/D_c=2.5. By comparison with measurements at the z/D_c=2.0 location, it is confirmed that near wall effects are avoided. Six repeatable trials are conducted at 1 khz with 2562 frames per trial. Three separate Reynolds numbers are tested across the tunnel's operating range with the current examples constrained to the results of the lowest operating speed, providing a cylinder Reynolds number of 1.57×10^4.

(a)   (b)
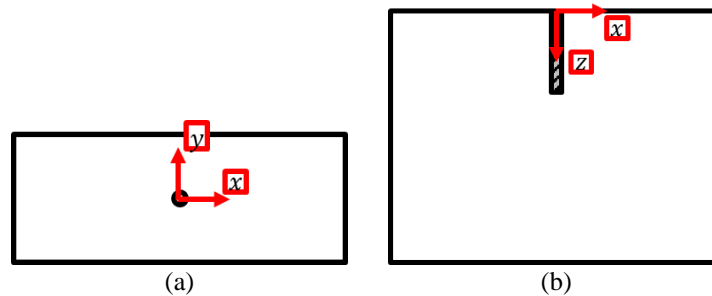
Figure 14: Coordinate system for flow past a cylinder experiments including (a) side view and (b) top view.

Investigation of the streamwise velocity is an imperative first effort in computational fluid dynamics validation. Directly reflecting all disruptions to the inlet boundary condition, observation of trends in the streamwise velocity profiles are clear indication of a transfer of momentum from the primary flow direction. These inferences provide the basis from which all other two or three-dimensional aspects of the flow's momentum can be addressed. Velocity profiles in the wake region of each cylinder are collapsed and presented in Figure 15 for each of the three geometries. Velocities and corresponding total uncertainties are non-dimensionalized according to the minimum tunnel operating bulk velocity, U_∞= 9.52 m^{1}s^{-1}.

From Figure 15(a), profile shapes at the x/D=1 location show a significant decrease in the freestream velocity and a change in sign in the immediate vicinity of the cylinders (-0.5 $\leq y/D \leq$ 0.5) as a result of the recirculation region. The square and hexagonal cylinders share nearly identical profiles at the x/D=2 location, after which the hexagonal shape shows the most significant drop in magnitude for the remaining profiles in the range 3 $\leq x/D \leq$ 6. In general, the round cylinder shows the narrowest wake, as clearly identified at all available traces. It is reasonable to assume that this is a result of the lack of edge features that the remaining two geometries share. All three shapes exhibit a return to the freestream condition at the x/D=6 position, as signified by a "flatting" of the profiles or more explicitly, $\langle U \rangle / U_\infty \rightarrow$ 1 at each spanwise position. As expected, the round cylinder provides the flattest profile at the x/D =6 location, and conversely, the hexagon provides the greatest divergence. It would seem that the inclusion of additional sides and corners has enabled further turbulence generation that extended further downstream in comparison to that of the square cylinder.

The uncertainty profiles presented in Figure 15(b) complete the current evaluation of the benchmark case. It is well understood that gradients in the flow that occur at scales beneath the final pass of the PIV interrogation window (in this case 32 × 32 pixels) are poorly captured, contributing to higher uncertainties in these areas. In general, uncertainties across all three cylinder types are largely found to be <12.5%, with the only offender being the square. The square geometry produces the widest wake and corresponding shear layers contributing to the peaks in the x/D=1 and 2 profiles. It is believed that the vortical structures produced by the square in the near field are substantially smaller than that of their round or hexagonal counterparts as well, contributing to the peaks found for the x/D=3 and 4 profiles. In future work, vortex identification algorithms should be employed to confirm these results.
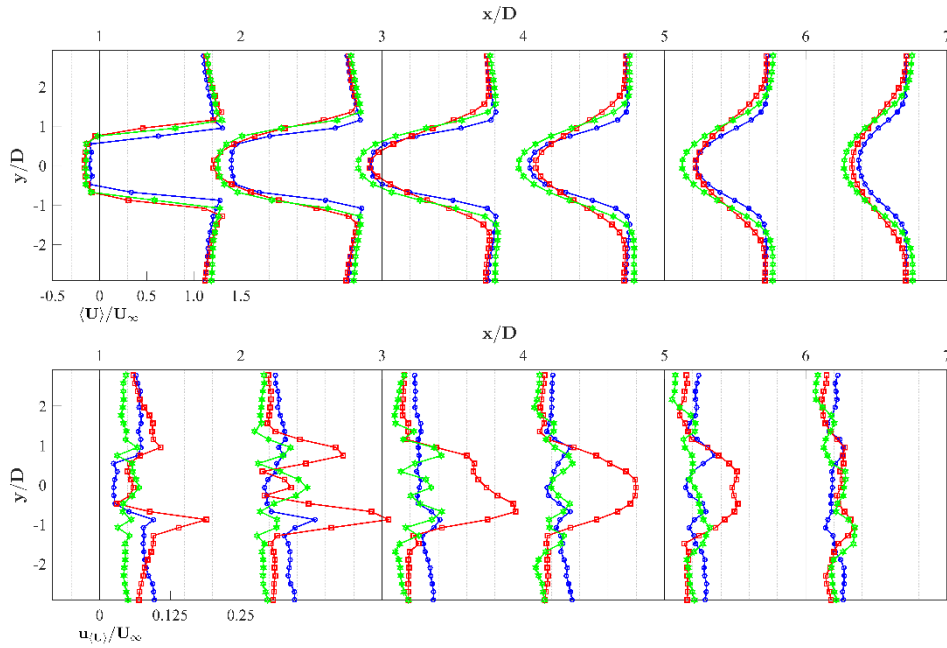
Figure 15: Spanwise profiles of the cylinder wake (a) ensemble averaged velocity component $\langle U \rangle / U_\infty$ and (b) corresponding total uncertainty, $u_{\langle U \rangle} \backslash U_\infty$. Legend: ⭕ - round, ⬜ - square, ✿ - hexagon.

Fluid stresses consist of three main contributors, namely: (1) the viscous stress, (2) the isotropic stress $-\langle p \rangle \delta_{ij}$ from the mean pressure field, and (3) $-\rho \langle u_i u_j \rangle$ arising from fluctuations in the velocity field as a result of turbulence[29]. For velocity measurements, it is convenient to drop the density term, usually under the pretense of incompressible flow, at which point the remaining $\langle u_i u_j \rangle$ terms are referred to as the Reynolds stresses. A significant part of the equations for the mean field, the Reynolds stresses serve as another validation metric of interest. This, along with the ensembled averaged velocities, serves as the fundamental metrics for comparison to Reynolds-Averaged Navier-Stokes (RANS) equations. The Reynold stresses comprise a second-order symmetric tensor, whose diagonal components form the normal stresses and whose off diagonal components form the shear stresses. In general, the shear stresses are harder to model and simulate: two separate velocity components comprise the shear stresses, calculated as the covariance, with independent magnitudes and uncertainties. The Reynolds shear stress profiles for the current benchmark are presented in Figure 16. As expected, there is near perfect symmetry across y/D=0 for each trace as a result of the spanwise fluctuating velocity component, v, changing sign. At the x/D=1 trace, the profiles exhibit almost evenly spaced magnitudes, where the square generates the largest peaks and the round exhibits the smallest. Across all profiles considered, the square profiles exhibit distinct maximum peaks at the x/D=3 location, as opposed to the round and hexagonal cylinders exhibiting their maximums at x/D=4. As echoed by observations of the streamwise velocity component, with increasing downstream distance ($4 \leq x/D \leq 6$), the hexagonal profiles seem to more closely represent the square than that of the round cylinder. In this region, the hexagonal cylinder exhibits slightly smaller magnitudes with narrow profiles than the square, but is otherwise identical in shape.
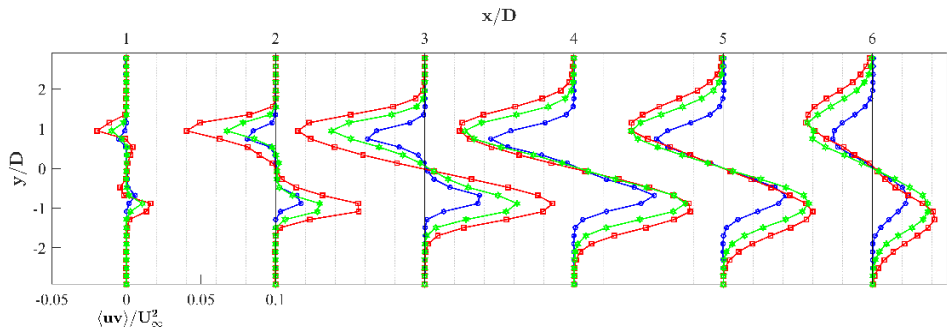
Figure 16: Spanwise profiles of the cylinder wake Reynolds shear stress profiles, $\langle uv \rangle / U_\infty$. Legend is identical to Figure 15.

Higher fidelity simulations, i.e., Large Eddy Simulation (LES) or Direct Numerical Simulation (DNS) are able to leverage additional forms of experimental validation due to their rich temporal resolution. Even in time resolved PIV systems, typical sampling frequencies for commercial hardware are in the neighborhood of 1-2 khz, paling in comparison to the theoretically limitless frequency content of LES or DNS data sets. From the validation perspective, PIV measurements and the general class of optical measurements are best suited for their spatial content. An increasingly popular way of assuaging experimental limitations, and still in indicative of the temporal content of the physics, is the use of model order reduction. The current examples utilized the proper orthogonal decomposition (POD) in accordance with the hard threshold truncation methods of Gavish and Donoho [42].

The eigenvectors, or spatial mode shapes, for the first four modes for the streamwise velocity, U, of each cylinder are presented in Figure 17. To the best of the authors' knowledge, this is the first time a hexagonal cylinder's spatial mode shapes have been presented (Figure 17(c)). The measurement data is directly used as the input X for the POD calculation, in other words, the data is not mean subtracted. This is reaffirmed from the first mode shape, ψ_1, of each cylinder resembling a qualitatively identical shape to that of the average velocity field for each cylinder. It should be noted that all displayed modes greater than one use a fixed (universal) color bar for visual comparison. Interestingly, the following pairs show nearly identical shapes: hex-ψ_2 and round-ψ_3, hex-ψ_3-square-ψ_2, and hex-ψ_4 and square-ψ_2. From these observations of the decomposition, all three of the geometries exhibit different combinations of the same large scale features of kinetic energy. This notion suggests that for a given free stream Reynolds number, the cylinder cross section plays a vital part in the distribution of kinetic energy. By understanding the dominant coherent structures as a function of cylinder cross section, shearing and vortical formation of the bluff body wake can be better understood and controlled in application.
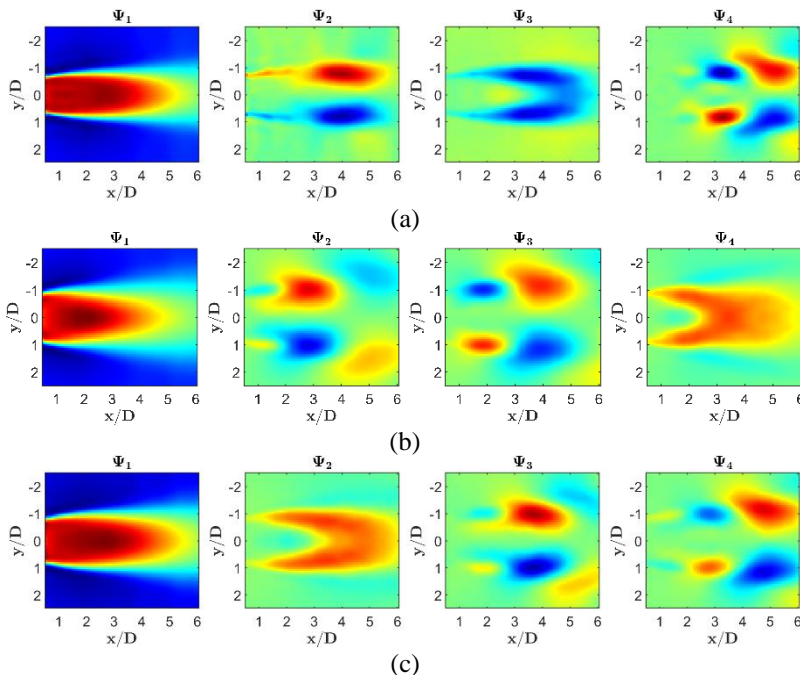
Figure 17: POD mode shapes, or eigenvectors, for the (a) round, (b) square, and (c) hexagonal cylinder.
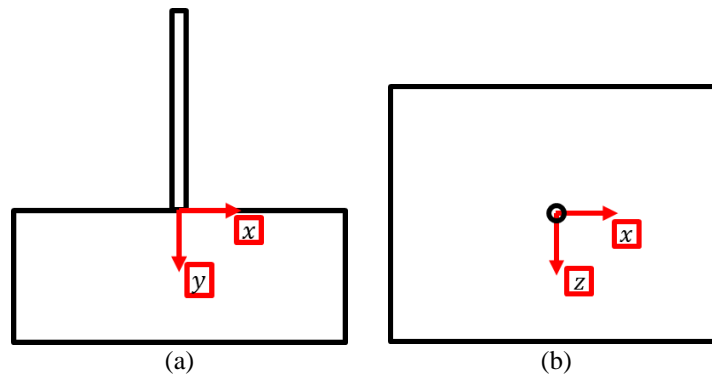
4.2 Jet in Cross Flow

The jet in cross flow, or transverse jet, represents another canonical flow type found in a variety of applications. The most commonly recognized scenario is a round jet with bulk velocity, V_j, issuing perpendicularly from a wall into a cross flow, U_∞. Interest stems from the flow's superior mixing and dispersion characteristics when compared to a free jet. The jet in cross flow has received a rich and ongoing history spanning some 60 years [43]. Though typically studied as a unit problem, the jet in cross flow is employed in multiple arrays in application. In propulsion, they are used for fuel or dilution air injection in air breathing engines and for thrust vector control in vehicle guidance, navigation, and control [44]. In power generation, they serve as a coolant transport mechanism for the prismatic high temperature gas reactor [45]. In turbomachinery, recent advances in 3D printing have produced high pressure turbine blades designed with passive film cooling for increased efficiency [46]. Even in nature, the interaction of wind currents with volcanic mountain wakes are the culprit for unusual changes in local atmosphere and soil content [47]. From the design perspective, current interests involve jet placement (flush with or protruding from wall), angled injection, and the shape of the jet itself, and how these geometric features influence hydraulic, thermal, and chemical mixing across all flow regimes. Indeed, a wide variety of motivations exist for the jet in cross flow, however our interest here is limited to incompressible, low speed applications. In general, the current facility is capable of jet to cross flow velocity ratios in the range of approximately $0.9 \leq V_j/U_\infty \leq 1.7$.

Immediately at the jet exit, there exists an adverse pressure gradient on the windward (upstream) side of the jet as a result of the interaction with the cross flow as confirmed by both hotwire experiments from Kelso et al. [48] and DNS simulations by Muppidi and Mahesh [49]. As a result of mass conservation, the jet experiences a skewed exit velocity profile, shifted towards the leeward (downstream) side of the jet. The incurred vortex formation is primarily a function of the jet to cross flow ratio. Two major types of coherent vortex systems have been identified for jet to cross flow ratios greater than unity [50]. The most dominant type is the counter rotating vortex pair. Many experimental and numerical efforts have sought to explain the highly unsteady and asymmetric features of the counter rotating vortex pair from which it is clear no universal behavior exists for all jet to cross flow ratios. The general consensus is that the counter rotating vortex pair is caused by the cross flow's influence on the jet vorticity initiated in the near field [51],[52],[53]. The second type of coherent vortex system consists of smaller horseshoe and wake vortices. These features develop in the leading edge of the jet as a result of the crossflow boundary layer's interaction with the adverse pressure gradient, which separates in the spanwise

direction, forming a trail of vortices around and downstream of the jet. Kelso et al.'s results confirm that these features can be steady, oscillate, or coalesce depending on the velocity ratio [54]. Gopalan et al. used wall mounted pressure sensors and PIV to determine that the wall pressure fluctuations on the windward side of the jet increase until $V_j/U_\infty > 2$ at which point the near-wall flow's effect diminishes [55]. These coherent vortex systems are of primary and ongoing interest, particularly in more complicated arrays found in application. We first introduce our rendition of the canonical jet in cross flow experiment, with particular emphasis on the hydraulic features of the flow. Such benchmark quantities are critical towards explaining more complicated features of the vortex dynamics in more convoluted arrays. Ongoing with the theme of this section, these initial results also serve as fundamental validation benchmarks towards future numerical contributions which aim to achieve like-minded insights into the physics of repetitive transverse jet geometries and their interactions.

As with Section 4.1, the coordinate system is re-oriented again, now in compliance with the majority of jet in cross flow literature. The circular jet is mounted and centered on the ceiling of the test section. The x^+ prescribes the cross-flow direction, y^+ pertains to the primary jet motion, and the z-direction constitutes the spanwise spread of the jet as seen in Figure 18. The jet's axial centerline point on the ceiling of the test section is the origin of the coordinate system. Two-dimensional, time-resolved PIV measurements are captured in both the xy center plane and the xz plane at the x/D_j=1 location, where the jet diameter is D_j= 22.225 mm. For the xy plane, a total of 2600 frames at 1 kHz are captured with six repeatable trials for each case. The same recording parameters are used for the xz plane for one trial. Five separate jet to cross flow velocity ratios are tested (V_j/U_∞ = 0.92, 1.05, 1.26, 1.48, 1.70), with the cross flow held constant at U_∞= 9.52 m/s. The current example focuses on the V_j/U_∞ = 0.92, 1.26, 1.70 cases specifically.


(a)   (b)

Figure 18: Coordinate system for the jet in cross flow experiments including (a) side view and (b) top view.

The transverse velocity, V, represents the major motion of the fluid along the jet's axis. As displayed in Figure 19, the magnitude of this component, and how it varies as a function of y, can best be interpreted as the jet's penetration into the free stream. With increasing downstream distance, its magnitude decreases, a clear indicator that the momentum is transferred to the streamwise and spanwise coordinates. From Figure 19, it is clear the jet penetration is dependent on the jet inlet Reynolds number. The x/D_j=0 trace provides the largest discrepancy in peak magnitudes, as expected. The highest ratio case promotes the largest gradients in its profile across all available profiles. With downstream distance, the highest ratio case causes the largest spread in profile with respect to the y direction, but in general the same maxima and minima shapes are exhibited across all cases. It is interesting to see that while one peak is found at the x/D=0 location, a secondary peak occurs for all traces downstream, no doubt as a function of the wake recirculation promoted by each case. From Figure 19(b), it is clear that with the exception of one point for the V_j/U_∞ = 1.26 case, all uncertainties are found to be less than 12.5%.
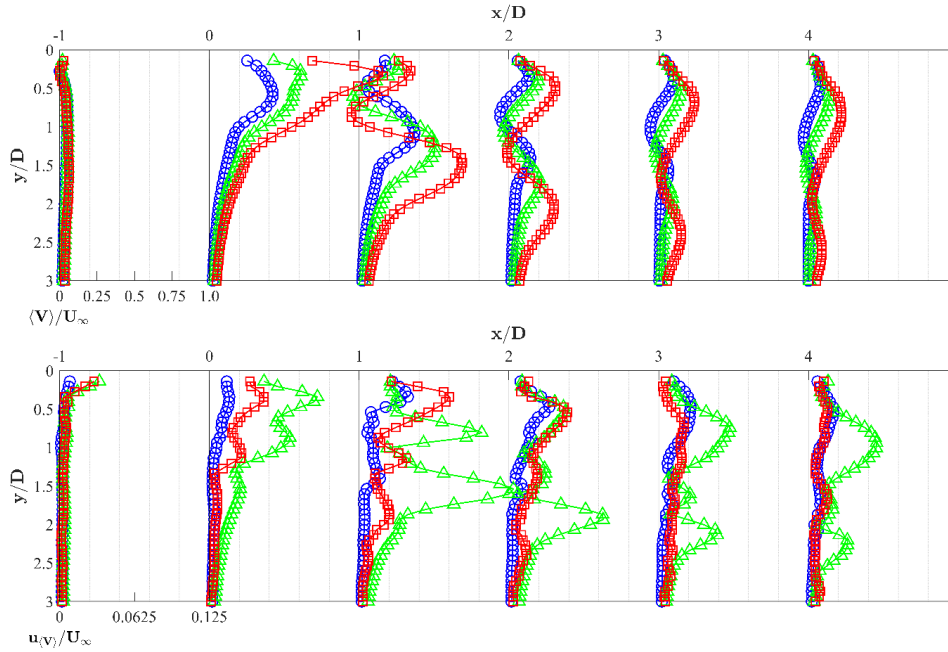
Figure 19: Spanwise profiles of the jet in cross flow (a) ensemble averaged velocity component $\langle V \rangle / U_\infty$ and (b) corresponding total uncertainty, $u_{\langle V \rangle} \backslash U_\infty$. Legend: ○ - V_j/U_∞ =0.92, △ - V_j/U_∞ =1.26, □ - V_j/U_∞ =1.70.

Reynolds shear stress profiles for the jet in cross flow are presented in Figure 20. Shear stresses reach a maximum in the immediate vicinity of the jet as a result of the immediate perturbation of the jet into the free stream. Though narrow in this immediate region, the peak and corresponding minimum are spread with increasing downstream distance. It is also clear that the positive shear found in the wake region decreases with downstream distance. Conversely, the negative shear found in the free stream grows in magnitude with downstream distance, as the effect of shearing penetrates further into the cross flow. With increasing velocity ratio, these peaks and their spread are increasing similarly to the observations for the transverse velocity discussed previously. These observations are good indication of potential applications in control of the transverse jet's mixing with the free stream and corresponding wake formation.
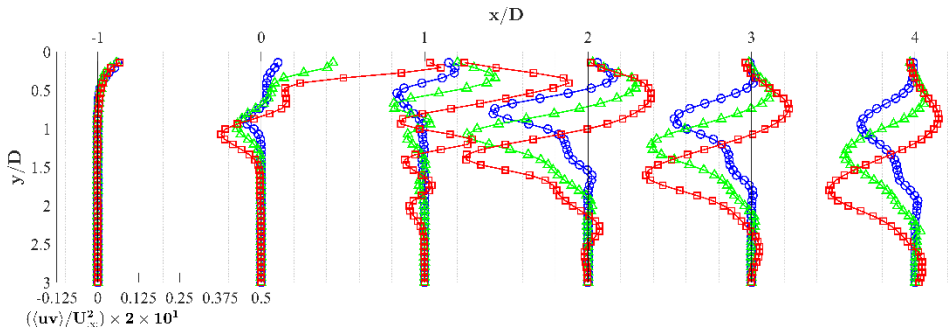
Figure 20: Spanwise profiles of the jet in cross flow Reynolds shear stress profiles, $\langle uv \rangle / U_\infty$. Legend is identical to Figure 19.

The section concludes with investigation of the eigenvectors of streamwise velocity promoted by each case in the xz plane, presented in Figure 21. The first column constitutes the mean field of each case from which the general shape of the wake and a reoccurring bubble region can be found upstream. The bubble is a result of the boundary layer interaction on the windward side and the wake region is induced by recirculation of the fluid behind the immediate jet penetration into the cross flow. The second eigenvector (second column) provides a consistent behavior across each case, constituting the major convective motion as a result of shear in the spanwise direction. Perhaps more interesting are the inconsistent behaviors found in modes three and four, found in the third and fourth columns respectively. In general, these areas can be categorized as single (i.e., Figure 21(a)ψ_3, Figure 21(a)ψ_4, Figure 21(a)ψ_3) and multi-structured regions (i.e., Figure 21(a)ψ_4, Figure 21(a)ψ_3, Figure 21(a)ψ_4). The single structures are best interpreted as a larger recirculation pocket, while the multi-shaped regions are more indicative of the action of symmetric vortical structures. It is interesting to see that no clear trends are found for the third and fourth spatial modes, hinting that different convective mechanisms are dictating the kinetic energy content as a function of velocity ratio and penetration into the free stream. It is also possible that these profiles are shared across all velocity ratios at differing xz planar locations. Prescribing these mechanisms is of considerable interest to the fluid mechanics community, with ongoing reduced order modeling efforts to better understand the influence of boundary layer interactions and vortical formation of the jet in cross flow.
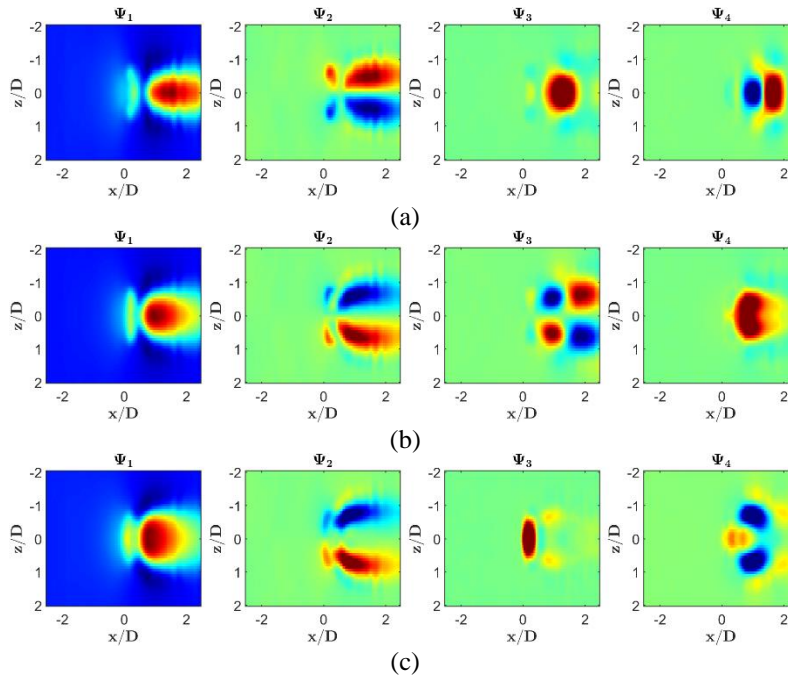
Figure 21: POD mode shapes, or eigenvectors, for the (a) V_j/U_∞ =0.92, (b) V_j/U_∞ =1.26, (c) V_j/U_∞ =1.70 case.

5.0 CONCLUSIONS

The Thermal Hydraulics Verification and Validation (THVV) Laboratory's low speed wind tunnel has been reconstructed at Texas A&M University. Several modifications to the original design have been motivated by recently acquired high speed optical diagnostics equipment. The upgrades have promoted a renewed interest in assessing the capabilities and flow quality of the tunnel. Inlet velocity profiles, inlet temperature profiles, and test section pressure readings serve to provide a first fundamental basis for fully constraining thermal fluid experiments anticipated for this facility. The report immediately serves the experimentalist in ensuring accurate test capabilities and fluid property correlations. The results are also intended to serve analogous computational model inputs including inlet conditions, boundary conditions, fluid properties, and turbulence parameters for model closure. The article closes with the results of preliminary experiments based on two canonical flow types: flow past a cylinder and the jet in cross flow. The results are presented succinctly as validation data including ensemble averaged velocities, Reynold stresses, and POD eigenvectors. The preliminary experiments are of interest to a current experimental campaign underway in the laboratory, involving more complex combinations of the two unit flow types.

ACKNOWLEDGMENTS

REFERENCES

[1] Landfried, D. T., Kristo, P., Clifford, C. E., and Kimber, M., 2019, "Design of an experimental facility with a unit cell test section for studies of the lower plenum in prismatic high temperature gas reactors," Annals of Nuclear Energy, 133, pp. 236-247.

[2] Landfried, D. T., 2015, "Experimental and Computational Studies of Thermal Mixing in Next Generation Nuclear Reactors," Doctorate of Philosophy, University of Pittsburgh, Pittsburgh, PA, USA.

[3] Reshotko, E. S., W.S., and Nagib, H. M., 1997, "Flow quality issues for large wind tunnels," 35th Aerospace Sciences Meeting & ExhibitReno, NV, USA.

[4] Saric, W., and Reshotko, E., 1998, "Review of flow quality issues in wind tunnel testing," 20th AIAA Advanced Measurement and Ground Testing Technology Conference. 1998Albuquerque, NM, USA.

[5] Quinn, D. B., Watts, A., Nagle, T., and Lentink, D., 2017, "A new low-turbulence wind tunnel for animal and small vehicle flight experiments," Royal Society Open Science, 4(3), p. 160960.

[6] Premi, A., Maughmer, M., and Brophy, C., 2012, "Flow-Quality Measurements and Qualification of the Pennsylvania State University Low-Speed, Low-Turbulence Wind Tunnel," 50th AIAA Aerospace Sciences Meeting including the New Horizons Forum and Aerospace ExpositionNashville, TN, USA.

[7] Moffat, R. J., 1988, "Describing the Uncertainties in Experimental Results," Experimental Thermal and Fluid Science, 1(1), pp. 3-17.

[8] (ASME), A. S. o. M. E., 2005, "Test Uncertainty."

[9] (ASME), A. S. o. M. E., 2009, "Standard for Verification and Validation in Computational Fluid Dynamics and Heat Transfer."

[10] Oberkampf, W. L., and Smith, B. L., 2017, "Assessment Criteria for Computational Fluid Dynamics Model Validation Experiments," Journal of Verification, Validation, and Uncertainty Quantification, 2(3), p. 031002.

[11] Barlow, J. B., Rae, W. H., and Pope, A., 1999, Low-Speed Wind Tunnel Testing, John Wiley & Sons, Inc.

[12] Mehta, R. D., and Bradshaw, P., 1979, "Design rules for small low speed wind tunnels," The Aeronatical Journal, 83(827), pp. 443-453.

[13] Coleman, H. W., and Steele, W. G., 2009, Experimentation, Validation, and Uncertainty Analysis for Engineers, John Wiley & Sons, Inc.

[14] Scheiman, J., and Brooks, J. D., 1981, "Comparison of experimental and theoretical turbulence reduction from screens, honeycomb, and honeycomb-screen combinations," Journal of Aircraft, 18(8), pp. 638-643.

[15] Mehta, R. D., 1985, "Turbulent Boundary Layer Perturbed by a Screen," AIAA Journal, 23(9), pp. 1335-1342.

[16] Bell, J. H., and Mehta, R. D., 1988, "Contraction design for small low-speed wind tunnels," N. A. a. S. Administration, ed.

[17] Shafi, I. T., Kristo, P., Weiss, A. G., and Kimber, M. L., "Qualitative Approaches to Understanding Coherent Structures in Turbulence," Proc. 72nd Annual Meeting of the APS Division of Fluid Dynamics.

[18] Reed, R. S., Weiss, A. W., Kristo, P., and Kimber, M. L., 2020, "Hydraulic Comparison of Single and Multiple-Jet Impingement on a Flate Plate," 5th Thermal and Fluids Engineering Conference (TFEC), ASTFE Digital Library, Virtual.

[19] Lewandowski, M., Kristo, P., Weiss, A., and Kimber, M. L., 2020, "Comparison of the Behavior of Different Jet Configuraitons in a Crossflow," ASME 28th International Conference on Nuclear Engineering (ICONE 28)Virtual.

[20] Taylor, A. M. K. P., Whitelaw, J. H., and Yianneskis, M., 1981, "Turbulent Flow in a Square-to-Round Transition," N. A. a. S. A. (NASA), ed.

[21] Sciacchitano, A., Neal, D. R., Smith, B. L., Warner, S. O., Vlachos, P. P., Wieneke, B., and Scarano, F., 2015, "Collaborative framework for PIV uncertainty quantification: comparative assessment of methods," Measurement Science and Technology, 26(7), p. 074004.

[22] Neal, D. R., Sciacchitano, A., Smith, B. L., and Scarano, F., 2015, "Collaborative framework for PIV uncertainty quantification: the experimental database," Measurement Science and Technology, 26(7), p. 074003.

[23] Wieneke, B., 2015, "PIV uncertainty quantification from correlation statistics," Measurement Science and Technology, 26(7), p. 074002.

[24] Sciacchitano, A., and Wieneke, B., 2016, "PIV uncertainty propagation," Measurement Science and Technology, 27(8), p. 084006.

[25] Figliola, R. S., and Beasley, D. E., 2011, Theory and Design for Mechanical Measurements, John Wiley and Sons, Inc.

[26] Dular, M., Bachert, R., Stoffel, B., and Širok, B., 2008, "Influence of the velocity distribution at the inlet boundary on the CFD prediction of local velocity and pressure fields around a hydrofoil," Experimental Thermal and Fluid Science, 32(3), pp. 882-891.

[27] Bradshaw, P., 1971, An introduction to turbulence and its measurement: thermodynamics and fluid mechanics series, Elsevier.

[28] Hunt, L., Downs, R., Kuester, M., White, E., and Saric, W., 2010, "Flow Quality Measurements in the Klebanoff-Saric Wind Tunnel," 27th AIAA Aerodynamic Measurement Technology and Ground Testing ConferenceChicago, IL, USA.

[29] Pope, S. B., 2000, Turbulent Flows, Cambridge University Press.

[30] Sirovich, L., 1987, "Turbulence and the dynamics of coherent structures. I. Coherent structures," Quarterly of Applied Mathematics, 45(3), pp. 561-571.

[31] Sirovich, L., 1987, "Turbulence and the dynamics of coherent structures. II. Symmetries and transformations," Quarterly of Applied Mathematics, 45(3), pp. 573-582.

[32] Sirovich, L., 1987, "Turbulence and the dynamics of coherent structures. III. Dynamics and scaling," Quarterly of Applied Mathematics, 45(3), pp. 583-590.

[33] Holmes, P., Lumley, J. L., Berkooz, G., and Rowley, C. W., 2012, Turbulence, Coherent Structures, Dynamical Systems and Symmetry, Cambridge University Press.

[34] Brunton, S. L., and Kutz, J. N., 2019, Data-driven science and engineering: Machine learning, dynamical systems, and control, Cambridge University Press.

[35] Kutz, J. N., Brunton, S. L., Brunton, B. W., and Proctor, J. L., 2016, Dynamic mode decomposition: data-driven modeling of complex systems, Society for Industrial and Applied Mathematics.

[36] Williamson, C. H. K., 1996, "Vortex Dynamics in the Cylinder Wake," Annual Review of Fluid Mechanics, 28(1), pp. 477-539.

[37] Bai, H., and Alam, M. M., 2018, "Dependence of square cylinder wake on Reynolds number," Physics of Fluids, 30(1).

[38] Sparrow, E. M., Abraham, J. P., and Tong, J. C. K., 2004, "Archival correlations for average heat transfer coefficients for non-circular and circular cylinders and for spheres in cross-flow," International Journal of Heat and Mass Transfer, 47(24), pp. 5285-5296.

[39] Hilpert, R., and Forsch., 1933, "Warmeabgabe von heheizten drahten und rohrem im luftsstrom," Gebiete Ing.-Wesen, pp. 215-224.

[40] Khaledi, H. A., and Andersson, H. I., 2011, "On vortex shedding from a hexagonal cylinder," Physics Letters A, 375(45), pp. 4007-4021.

[41] Tian, Z. W., and Wu, Z. N., 2009, "A study of two-dimensional flow past regular polygons via conformal mapping," Journal of Fluid Mechanics, 628, pp. 121-154.

[42] Gavish, M., and Donoho, D. L., 2014, "The Optimal Hard Threshold for Singular Values is $4/\sqrt{3}$," IEEE Transactions on Information Theory, 60(8), pp. 5040-5053.

[43] Ruggeri, R. S., Callaghan, E. E., and Bowden, D. T., 1950, "Penetration of air jets issuing from circular, square, and elliptical orifices directed perpendicularly to an air stream," N. A. C. f. Aeronautics, ed., Lewis Flight Propulsion Laboratory, Cleveland, OH, USA.

[44] Karagozian, A. R., 2010, "Transverse jets and their control," Progress in Energy and Combustion Science, 36(5), pp. 531-553.

[45] Amini, N., and Hassan, Y. A., 2009, "Measurements of jet flows impinging into a channel containing a rod bundle using dynamic PIV," International Journal of Heat and Mass Transfer, 52(23-24), pp. 5479-5495.

[46] Bons, J. P., Sondergaard, R., and Rivir, R. B., 2002, "The Fluid Dynamics of LPT Blade Separation Control Using Pulsed Jets," Journal of Turbomachinery, 124(1), pp. 77-85.

[47] Gardner, J. E., Burgisser, A., and Stelling, P., 2007, "Eruption and deposition of the Fisher Tuff (Alaska): evidence for the evolution of pyroclastic flows," The Journal of Geology, 115, pp. 417-435.

[48] Kelso, R. M., Lim, T. T., and Perry, A. E., 1996, "An experimental study of round jets in a cross-flow," Journal of Fluid Mechanics, 306, pp. 111-144.

[49] Muppidi, S., and Mahesh, K., 2005, "Study of trajectories of jets in crossflow using direct numerical simulations," Journal of Fluid Mechanics, 530, pp. 81-100.

[50] Mahesh, K., 2013, "The Interaction of Jets with Crossflow," Annual Review of Fluid Mechanics, 45(1), pp. 379-407.

[51] Andreopoulos, J., and Rodi, W., 1984, "Experimental investigation of jets in a crossflow," Journal of Fluid Mechanics, 138, pp. 93-127.

[52] Coelho, S. L. V., and Hunt, J. C. R., 1989, "The dynamics of the near field of strong jets in crossflows," Journal of Fluid Mechanics, 200, pp. 95-120.

[53] Sykes, R. I., Lewellen, W. S., and Parker, S. F., 1986, "On the vorticity dynamics of a turbulent jet in a crossflow," Journal of Fluid Mechanics, 168.

[54] Kelso, R. M., and Smits, A. J., 1995, "Horseshoe vortex systems resulting from the interaction between a laminar boundary layer and a transverse jet," Physics of Fluids, 7(1), pp. 153-158.

[55] Gopalan, S., Abraham, B. M., and Katz, J., 2004, "The structure of a jet in cross flow at low velocity ratios," Physics of Fluids, 16(6), pp. 2067-2087.